

Manifold constrained joint sparse learning via non-convex regularization

Jingjing Liu^{a,d,1}, Xianchao Xiu^{b,1}, Xin Jiang^a, Wanquan Liu^c, Xiaoyang Zeng^a, Mingyu Wang^{a,*}, Hui Chen^e

^a State Key Laboratory of ASIC and System, School of Microelectronics, Fudan University, Shanghai, China

^b School of Mechatronic Engineering and Automation, Shanghai University, Shanghai, China

^c School of Intelligent Systems Engineering, Sun Yat-sen University, Guangzhou, China

^d School of Computer Science and Technology, Shanghai University of Electric Power, Shanghai, China

^e School of Automation Engineering, Shanghai University of Electric Power, Shanghai, China

ARTICLE INFO

Article history:

Received 22 September 2020

Revised 31 March 2021

Accepted 3 June 2021

Available online 05 June 2021

Communicated by Zidong Wang

Keywords:

Robust principal component analysis (RPCA)
Manifold constrained joint sparse learning (MCJSL)

Non-convex regularization
Manifold alternating direction method of multipliers

ABSTRACT

The traditional robust principal component analysis (RPCA) via decomposition into low-rank plus sparse matrices offers a powerful framework for a large variety of applications in computer vision. However, the reconstructed image experiences serious interference by Gaussian noise, resulting in the degradation of image quality during the denoising process. Thus, a novel manifold constrained joint sparse learning (MCJSL) via non-convex regularization approach is proposed in this paper. Morelly, the manifold constraint is adopted to preserve the local geometric structures and the non-convex joint sparsity is introduced to capture the global row-wise sparse structures. To solve MCJSL, an efficient optimization algorithm using the manifold alternating direction method of multipliers (MADMM) is designed with closed-form solutions and it achieves a fast and convergent procedure. Moreover, the convergence is analyzed mathematically and numerically. Comparisons among the proposed MCJSL and some state-of-the-art solvers, on several accessible datasets, are presented to demonstrate its superiority in image denoising and background subtraction. The results indicate the importance to incorporate the manifold learning and non-convex joint sparse regularization into a general RPCA framework.

© 2021 Elsevier B.V. All rights reserved.

1. Introduction

Robust principal component analysis (RPCA) is a popular topic in computer vision, which has been extensively applied in the fields such as image denoising and background subtraction [1–5]. Generally speaking, RPCA intends to discover a low-rank matrix to approximate the original noisy data well. For example, in background subtraction, the surveillance video can be decomposed into the sum of a background component and a foreground component. Since the background component has relatively static small changes over a period, it can be described as a low-rank matrix [6]. During the past decades, a large number of RPCA-related theories, algorithms, and applications have been proposed [7–12].

Specifically, given an original noisy image \mathbf{D} , RPCA intends to estimate the low-rank matrix \mathbf{L} and sparse matrix \mathbf{S} , with

$\mathbf{D} = \mathbf{L} + \mathbf{S}$. In the optimization of RPCA, Cai et al. [13] utilized the nuclear norm to estimate the low-rank matrix, which is called nuclear norm minimization (NNM). By applying a singular value thresholding, the original data matrix can be reconstructed effectively under certain conditions. However, NNM applies the same thresholding to shrink all the singular values, which does not consider the fact that the image information is mainly concentrated on the larger values. Therefore, the details of the image will become too smooth and blurred. To overcome this shortcoming, Gu et al. [14] proposed weighted nuclear norm minimization (WNNM), which integrates the weighted technique with non-negative matrix factorization (NMF). They proved that WNNM can obtain better approximation via numerical experiments in image denoising and background subtraction. It would not be exaggerating to express that WNNM has become one of the most prevalent methods to resolve the RPCA. Due to the rapid developments in non-convex optimization, one can further improve the performance of NNM-based RPCA by adding non-convex regularization terms [15–19]. The fundamental reason for this is the L_1 norm and nuclear norm of NNM-based RPCA are convex but with loose relaxations, which can not exploit the latent structures. Therefore, a tighter approximation can be pursued. Hu et al. [15] truncated

* Corresponding author.

E-mail addresses: liujingjing@fudan.edu.cn (Jingjing Liu), xcxiu@bjtu.edu.cn (X. Xiu), 19212020102@fudan.edu.cn (X. Jiang), W.Liu@curtin.edu.au (W. Liu), xy-zeng@fudan.edu.cn (X. Zeng), mywang@fudan.edu.cn (M. Wang), chenhui@shiep.edu.cn (H. Chen).

¹ These authors contributed equally to this paper.

the nuclear norm by removing small residuals, which enhances the robustness to noises. Quach et al. [16] replaced L_1 norm with L_p norm ($0 < p < 1$) and yielded a more sparse solution. Parekh et al. [17] presented a parameterized non-convex substitution to estimate the low-rank matrix, which can not only solve the low-rank minimization problem well but also achieve better results in image denoising. Chen [18] formulated a non-convex and non-separable regularization from a Bayesian perspective, which demonstrates encouraging performance in hyperspectral images. Wen et al. [19] considered a generalized nonconvex regularization, including L_p norm and other non-convex functions such as smoothly clipped absolute deviation and minimax concave penalty. Wang et al. [20] proposed to add non-convex penalty function and a weighted version to RPCA-based model, which is a better low-rank approximation for image denoising.

Unfortunately, these aforementioned RPCA-based methods may not be able to extract valuable features in high-dimensional settings. From the aspect of image denoising, each row is related to one specific feature. Hence, it is natural to consider joint sparsity (i.e., $L_{2,1}$ norm) rather than L_1 norm. In order to facilitate better interpretations of selected features, joint sparsity is constructed by imposing $L_{2,1}$ norm constraints on variables [21,22]. It is illustrated that the joint sparsity can force the features not included in the projected space to be zero rows, which reduces the influence of outliers and abandons invalid features. Consequently, RPCA based on joint sparsity shares both the advantages of sparsity methods over dimension reduction methods, and over other RPCA-based methods.

Actually, if the samples in the high-dimensional space are distributed on the low-dimensional manifolds, it is easy to capture the low-level structures through RPCA-based methods. However, this assumption can not be effectively guaranteed in real-world applications. Inspired by recent advances of manifold learning, manifold constraints can be considered to maintain local geometric structures embedded in the high-dimensional space [23]. Enforcing manifold constraints always provides significant improvements in image denoising when one maps the original data onto a well-designed space [24]. Recently, Liu et al. [25] considered the manifold constrained RPCA, which takes advantages of manifold learning and RPCA. Compared with other kinds of RPCA, manifold constrained RPCA can both improve the performance of image reconstruction and reduce the running time. However, only manifold prior of the low-rank component is discussed, which leads to limited feature selection. Therefore, there is a need to construct a variant of RPCA that can extract meaningful features and preserve local geometric structures.

Motivated by the above work, a novel RPCA method based on the manifold constraint and non-convex joint sparse learning is proposed to improve the performance of image denoising and background subtraction in this paper. Since manifold constrained learning and joint sparse learning are employed, it is natural to abbreviate it as MCJSL, which to our knowledge has not been systematically analyzed elsewhere in the literature. As is illustrated in [26], compared with L_1 norm, $L_{1/2}$ norm is a better surrogate to measure the original sparsity. Thus, in this paper, a joint sparsity with $L_{2,1/2}$ norm is proposed by using L_2 norm to constrain intra-group structures and $L_{1/2}$ norm to constrain inter-group structures. To better illustrate the advantage of manifold constraint and $L_{2,1/2}$ regularization, Fig. 1 shows the framework of the proposed MCJSL. Here, white blocks indicate zero elements, gray blocks represent nonzero elements. It is observed that manifold learning is not only applied to the low-rank component, but also to the sparse component. In summary, manifold constrained learning preserves local geometric structures while non-convex joint sparse learning captures global geometric structures.

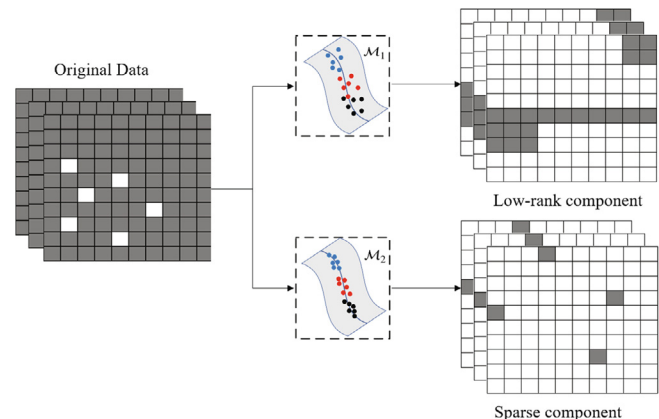


Fig. 1. Framework of the proposed MCJSL.

In comparison to previous analysis for RPCA-style methods, the merits of this paper can be distilled to the following three aspects:

- Novel manifold constrained model.** Instead of considering typical RPCA, a novel MCJSL method is proposed by introducing the manifold constraint and joint sparse learning via $L_{2,1/2}$ regularization. Actually, it is a very efficient framework for image denoising and background subtraction.
- Optimization algorithm.** An effective technique is developed to solve the proposed MCJSL, which is a non-convex constrained minimization problem, by utilizing the manifold alternating direction method of multipliers (MADMM). The resulting subproblems either can be solved by fast solvers or have closed-form solutions. Moreover, the convergence result is analyzed mathematically, which demonstrates that the proposed MCJSL is both efficient and convergent.
- Different computer vision applications.** For image denoising, compared with the up-to-date methods, the proposed MCJSL always obtains better performance with respect to peak signal-to-noise ratio (PSNR) and structural similarity (SSIM). For background subtraction, the proposed MCJSL also outperforms the traditional state-of-the-art methods in terms of F-score.

The remainder of this paper is organized as follows. Section 2 reviews RPCA and manifold learning. Section 3 establishes the proposed MCJSL with an efficient optimization algorithm. Section 4 implements MCJSL to complete image denoising task. Section 5 applies MCJSL to background subtraction. Finally, Section 6 concludes this paper.

2. Preliminaries

The purpose of RPCA is to estimate the potential low-rank matrix from its noisy input. Due to the inherent low-rank structure of data in many practical problems, RPCA has obtained great success in many computer vision applications. Here a brief review of the current improvement is provided for this subject. Firstly, a brief review of the fundamental models of RPCA is presented, then the manifold learning is described.

2.1. RPCA

Suppose that \mathbf{D} is the given observation data. Then RPCA aims to decompose \mathbf{D} into a low-rank matrix \mathbf{L} and a sparse matrix \mathbf{S} , which is in the form of

$$\begin{aligned} \min_{\mathbf{L}, \mathbf{S}} \quad & \text{rank}(\mathbf{L}) + \lambda \|\mathbf{S}\|_0 \\ \text{s.t.} \quad & \mathbf{D} = \mathbf{L} + \mathbf{S}, \end{aligned} \quad (1)$$

where $\|\cdot\|_0$ represents the number of non-zero elements, and $\lambda > 0$ is a tuning parameter. However, it is actually NP-hard due to the presence of $\text{rank}(\mathbf{L})$ and $\|\mathbf{S}\|_0$. Candès et al. [9] considered a variant by replacing rank with the nuclear norm (NNM) and $\|\cdot\|_0$ with L_1 norm, i.e.,

$$\begin{aligned} \min_{\mathbf{L}, \mathbf{S}} \quad & \|\mathbf{L}\|_* + \lambda \|\mathbf{S}\|_1 \\ \text{s.t.} \quad & \mathbf{D} = \mathbf{L} + \mathbf{S}, \end{aligned} \quad (2)$$

where $\|\cdot\|_*$ represents the nuclear norm, defined as the sum of all singular values. It is proved that if \mathbf{L} and \mathbf{S} satisfy certain conditions, problem (2) can accurately recover \mathbf{L} and \mathbf{S} , with a probability close to 1.

In fact, the nuclear norm is not the best convex relaxation for rank minimization. Recently, Gu et al. [14] proposed to utilize the weighted nuclear norm (WNNM) rather than conventional nuclear norm, and reformulated (2) as follows

$$\begin{aligned} \min_{\mathbf{L}, \mathbf{S}} \quad & \|\mathbf{L}\|_{\mathbf{w},*} + \lambda \|\mathbf{S}\|_1 \\ \text{s.t.} \quad & \mathbf{D} = \mathbf{L} + \mathbf{S}. \end{aligned} \quad (3)$$

Here $\|\cdot\|_{\mathbf{w},*}$ denotes the weighted nuclear norm, defined as $\|\mathbf{L}\|_{\mathbf{w},*} = \sum_i w_i \sigma_i(\mathbf{L})$, in which $\mathbf{w} = [w_1, \dots, w_n]^T$ is the non-negative weight vector, and $\sigma_i(\mathbf{L})$ is the i th largest singular value of matrix \mathbf{L} . In order to choose a proper weighted vector \mathbf{w} , they set w_i to be inversely proportional to $\sigma_i(\mathbf{L})$. The denoising results convince that WNNM is more effective to encourage low-rank solutions than NNM.

2.2. Manifold learning

Manifold learning, as a popular learning method, is often used to constrain local linear relations. Instead of using traditional Euclidean distance, Tenenbaum et al. [27] proposed to calculate the geodesic distance in differential geometry, which is called isometric feature mapping (ISOMAP). It guarantees the global optimal solution and high-speed computation. However, it has poor ability to expand manifolds with large internal curvature. Later, Chen et al. [28] proposed locally linear embedding (LLE) by assuming that the data are linear in smaller localities, i.e., all points can be linearly represented by several samples in their neighborhood. Accordingly, Liu et al. [25] applied the manifold learning technique (ManiDec) to explore the geometric characteristics of data distribution. The mathematical model is

$$\begin{aligned} \min_{\mathbf{L}, \mathbf{S}} \quad & \|\mathbf{L}\|_* + \lambda \|\mathbf{S}\|_1 \\ \text{s.t.} \quad & \mathbf{D} = \mathcal{E}(\mathbf{L} + \mathbf{S}), \mathbf{L} \in \mathcal{M}, \end{aligned} \quad (4)$$

which is equivalent to

$$\begin{aligned} \min_{\mathbf{L}, \mathbf{S}} \quad & \frac{1}{2} \|\mathbf{D} - \mathcal{E}(\mathbf{L} + \mathbf{S})\|_F^2 + \lambda_1 \|\mathbf{L}\|_* + \lambda_2 \|\mathbf{S}\|_1 \\ \text{s.t.} \quad & \mathbf{L} \in \mathcal{M}, \end{aligned} \quad (5)$$

where λ_1, λ_2 are the weights to balance the corresponding terms, \mathcal{E} is the transformation matrix, \mathcal{M} is a manifold constraint learned from given data, and $\mathbf{L} \in \mathcal{M}$ means that the clean images are reasonable presumed to lie on a manifold \mathcal{M} . It is verified that, compared with classical RPCA methods, ManiDec is able to improve the reconstruction ability by reducing shadows and noises.

3. Manifold constrained joint sparse learning

This section presents a novel method called MCJSL, which integrates the manifold constraints and non-convex joint sparsity into RPCA.

3.1. Model construction

It is known that L_1 norm may induce over-penalization while $L_{1/2}$ norm has nice nearly unbiased property and could overcome the drawbacks of L_1 norm [29]. In this regard, the L_1 norm in problem (5) can be replaced by $L_{1/2}$ norm if a more sparse solution is expected to be obtained. Therefore, by incorporating prior structure information, the manifold constrained joint sparse learning (MCJSL) is proposed as follows

$$\begin{aligned} \min_{\mathbf{L}, \mathbf{S}} \quad & \frac{1}{2} \|\mathbf{D} - \mathcal{E}(\mathbf{L} + \mathbf{S})\|_F^2 + \lambda_1 \|\mathbf{L}\|_{S_{1/2}}^{S_{1/2}} + \lambda_2 \|\mathbf{S}\|_{2,1/2} \\ \text{s.t.} \quad & \mathbf{L} \in \mathcal{M}_1, \mathbf{S} \in \mathcal{M}_2. \end{aligned} \quad (6)$$

Note that $\|\cdot\|_{S_{1/2}}$ is the matrix version of $L_{1/2}$ function, and $L_{2,1/2}$ is joint sparsity embedded by $L_{1/2}$ function, which is more efficient than $L_{2,1}$, and \mathcal{M}_1 and \mathcal{M}_2 are two manifolds to constrain \mathbf{L} and \mathbf{S} , respectively. It is worth noting that the combination of $L_{2,1/2}$ joint sparsity and manifold learning has not been considered previously. The usage of $L_{2,1/2}$ enjoys accurate determination of selected variables and fast optimization solvers. Moreover, the manifold \mathcal{M}_1 and \mathcal{M}_2 can preserve the local geometry of data.

3.2. Optimization algorithm for MCJSL

In this subsection, an optimization algorithm for solving the proposed MCJSL model (6) will be provided. To make use of its structure, we first introduce a new variable \mathbf{Z} and reformulate (6) as an equivalent constrained problem

$$\begin{aligned} \min_{\mathbf{L}, \mathbf{S}, \mathbf{Z}} \quad & \frac{1}{2} \|\mathbf{D} - \mathcal{E}(\mathbf{Z})\|_F^2 + \lambda_1 \|\mathbf{L}\|_{S_{1/2}}^{S_{1/2}} + \lambda_2 \|\mathbf{S}\|_{2,1/2} \\ \text{s.t.} \quad & \mathbf{L} \in \mathcal{M}_1, \mathbf{S} \in \mathcal{M}_2, \mathbf{Z} = \mathbf{L} + \mathbf{S}. \end{aligned} \quad (7)$$

The augmented Lagrange function of (7) is defined as

$$\begin{aligned} \mathcal{L}_\beta(\mathbf{L}, \mathbf{S}, \mathbf{Z}, \Lambda) = & \frac{1}{2} \|\mathbf{D} - \mathcal{E}(\mathbf{Z})\|_F^2 + \lambda_1 \|\mathbf{L}\|_{S_{1/2}}^{S_{1/2}} + \lambda_2 \|\mathbf{S}\|_{2,1/2} \\ & - \langle \Lambda, \mathbf{Z} - \mathbf{L} - \mathbf{S} \rangle + \frac{\beta}{2} \|\mathbf{Z} - \mathbf{L} - \mathbf{S}\|_F^2, \end{aligned}$$

where Λ is the Lagrange multiplier, and β is the positive penalty parameter. According to the manifold alternating direction method of multipliers (MADMM), the above problem can be effectively solved. Before discussing the resulting subproblems, the following lemmas should be reviewed.

Lemma 3.1. *The minimization problem*

$$\min_x \lambda |x|^{1/2} + \frac{1}{2} (x - t)^2$$

has a closed-form solution, which is given by the half thresholding operator defined as

$$x^* = \begin{cases} \mathcal{H}_{\lambda,1/2}(t) & \text{if } t > \frac{\sqrt{54}}{4} \lambda^{2/3}, \\ \{\mathcal{H}_{\lambda,1/2}(t), 0\} & \text{if } t = \frac{\sqrt{54}}{4} \lambda^{2/3}, \\ 0 & \text{if } t < \frac{\sqrt{54}}{4} \lambda^{2/3}, \end{cases}$$

where

$$\mathcal{H}_{\lambda,1/2}(t) = \frac{2}{3} t \left(1 + \cos \left(\frac{2\pi}{3} - \frac{2}{3} \varphi_\lambda(t) \right) \right)$$

with

$$\varphi_\lambda(t) = \arccos\left(\frac{\lambda}{8}\left(\frac{|t|}{3}\right)^{-3/2}\right).$$

Based on [Lemma 3.1](#), the following corollary can be developed which characterizes the closed-form solution for matrix cases.

Corollary 3.2. *The solution of*

$$\min_{\mathbf{X}} \lambda \|\mathbf{X}\|_{S_{1/2}}^{S_{1/2}} + \frac{1}{2} \|\mathbf{X} - \mathbf{T}\|_F^2,$$

can be described by the following matrix half thresholding operator

$$\mathbf{X}^* = \mathbf{U} \text{Diag}(\mathcal{H}_{\lambda,1/2}(\Sigma)) \mathbf{V}^T,$$

where $\Sigma = \text{Diag}(\sigma_1, \dots, \sigma_m)$ is the singular value decomposition (SVD) of \mathbf{T} , i.e., $\mathbf{T} = \mathbf{U} \Sigma \mathbf{V}^T$, and it has been proved in [\[30\]](#).

Lemma 3.3. *For minimization problem*

$$\min_{\mathbf{X}} \lambda \|\mathbf{X}\|_{2,1/2} + \frac{1}{2} \|\mathbf{X} - \mathbf{T}\|_F^2,$$

the closed-form solution is given by

$$\mathbf{X}^* = \mathcal{S}_{\lambda,1/2}(\mathbf{T}),$$

where

$$\mathcal{S}_{\lambda,1/2}(\mathbf{T}) = \mathcal{H}_{\lambda,1/2}(\mathbf{Y})$$

with

$$\mathbf{Y}_i^* = \frac{\mathbf{T}_i}{\|\mathbf{T}_i\|_2} \circ \max\{0, \|\mathbf{T}_i\|_2 - \lambda\},$$

where \mathbf{T}_i represents the i -th row of \mathbf{T} for $i = 1, \dots, m$. In fact, it is a combination of [Lemma 3.1](#) and [\[31\]](#).

By applying some simple linear algebraic transformations, we can obtain the following detailed update equation of each iteration.

- For variable \mathbf{L} , the optimization subproblem can be simplified to

$$\min_{\mathbf{L} \in \mathcal{M}_1} \lambda_1 \|\mathbf{L}\|_{S_{1/2}}^{S_{1/2}} + \frac{\beta}{2} \|\mathbf{Z}^k - \mathbf{L} - \mathbf{S}^k - \Lambda^k/\beta\|_F^2.$$

Actually, this computation contains two stages. In the first stage, according to [Corollary 3.2](#), the unconstrained subproblem is computed by

$$\mathbf{L}^{k+1/2} = \mathbf{U} \mathcal{H}_{\lambda_1/\beta,1/2}(\mathbf{Z}^k - \mathbf{S}^k - \Lambda^k/\beta) \mathbf{V}^T, \quad (8)$$

where \mathbf{U}, \mathbf{V} are the SVD of $\mathbf{Z}^k - \mathbf{S}^k - \Lambda^k/\beta$. In the second stage, the solution is refined by projecting onto the manifold \mathcal{M}_1 , that is to say,

$$\mathbf{L}^{k+1} = \Pi_{\mathcal{M}_1}(\mathbf{L}^{k+1/2}). \quad (9)$$

- For variable \mathbf{S} , the subproblem can be transformed as

$$\min_{\mathbf{S} \in \mathcal{M}_2} \lambda_2 \|\mathbf{S}\|_{2,1/2} + \frac{\beta}{2} \|\mathbf{Z}^k - \mathbf{L}^{k+1} - \mathbf{S} - \Lambda^k/\beta\|_F^2.$$

Similarly, we first compute

$$\mathbf{S}^{k+1/2} = \mathcal{H}_{\lambda_2/\beta,1/2}(\mathbf{Z}^k - \mathbf{L}^{k+1} - \Lambda^k/\beta), \quad (10)$$

and then

$$\mathbf{S}^{k+1} = \Pi_{\mathcal{M}_2}(\mathbf{S}^{k+1/2}). \quad (11)$$

- For variable \mathbf{Z} , the subproblem can be solved by

$$\mathbf{Z}^{k+1} = (\beta \mathbf{I} + \mathcal{E}^T \mathcal{E})^{-1} (\mathcal{E}^T \mathbf{D} + \mathbf{W}^k). \quad (12)$$

where \mathbf{W}^k is defined as $\mathbf{W}^k = \beta(\mathbf{L}^{k+1} + \mathbf{S}^{k+1}) + \Lambda^k$. Notice that the coefficient matrix $\beta \mathbf{I} + \mathcal{E}^T \mathcal{E}$ is nonsingular, thus it can be computed via common linear system solvers, such as the Cholesky decomposition and the conjugate gradient method.

- The update for dual variable Λ is

$$\Lambda^{k+1} = \Lambda^k - \beta(\mathbf{Z}^{k+1} - \mathbf{L}^{k+1} - \mathbf{S}^{k+1}). \quad (13)$$

Overall, the MADMM-based algorithm is proposed to solve problem [\(7\)](#) as shown in Algorithm 1.

Algorithm 1: MADMM for solving [\(7\)](#)

Input: Given data \mathbf{D} , parameters $\lambda_1, \lambda_2 > 0$;
Output: \mathbf{L}, \mathbf{S} ;

Initialize: Primal variables $\mathbf{Z}^0 = \mathcal{E}^T \mathbf{D}$ and $\mathbf{S}^0 = 0$, dual variable $\Lambda^0 = 0$, penalty parameter $\beta > 0$;

While not converge **do**

- 1: Update \mathbf{L}^{k+1} according to [\(8\)](#) and [\(9\)](#);
- 2: Update \mathbf{S}^{k+1} according to [\(10\)](#) and [\(11\)](#);
- 3: Update \mathbf{Z}^{k+1} according to [\(12\)](#);
- 4: Update Λ^{k+1} according to [\(13\)](#);

End while

3.3. Convergence analysis

The stationary point of problem [\(6\)](#) at the local minimizer $(\mathbf{L}^*, \mathbf{S}^*)$ is given by

$$\begin{cases} 0 \in \Pi_{\mathcal{M}_1}(-\mathcal{E}^T(\mathbf{D} - \mathcal{E}(\mathbf{L}^* + \mathbf{S}^*)) + \lambda_1 \partial \|\mathbf{L}^*\|_{S_{1/2}}^{S_{1/2}}); \\ 0 \in \Pi_{\mathcal{M}_2}(-\mathcal{E}^T(\mathbf{D} - \mathcal{E}(\mathbf{L}^* + \mathbf{S}^*)) + \lambda_2 \partial \|\mathbf{S}^*\|_{2,1/2}). \end{cases}$$

Then we present the first-order optimality conditions of the subproblems in Algorithm 1 as follows, which will be used repeatedly in the following convergence analysis.

$$\begin{cases} (a) \quad 0 \in \Pi_{\mathcal{M}_1}\left(\lambda_1 \partial \|\mathbf{L}^{k+1}\|_{S_{1/2}}^{S_{1/2}} + \Lambda^k - \beta(\mathbf{Z}^k - \mathbf{L}^{k+1} - \mathbf{S}^k)\right); \\ (b) \quad 0 \in \Pi_{\mathcal{M}_2}\left(\lambda_2 \partial \|\mathbf{S}^{k+1}\|_{2,1/2} + \Lambda^k - \beta(\mathbf{Z}^k - \mathbf{L}^{k+1} - \mathbf{S}^{k+1})\right); \\ (c) \quad 0 = -\mathcal{E}^T(\mathbf{D} - \mathcal{E}(\mathbf{Z}^{k+1})) - \Lambda^k + \beta(\mathbf{Z}^{k+1} - \mathbf{L}^{k+1} - \mathbf{S}^{k+1}); \\ (d) \quad \Lambda^{k+1} - \Lambda^k = -\beta(\mathbf{Z}^{k+1} - \mathbf{L}^{k+1} - \mathbf{S}^{k+1}). \end{cases}$$

Based on the above definition, we are now ready to prove our convergence result of Algorithm 1.

Theorem 3.4. Suppose $\{(\mathbf{L}^k, \mathbf{S}^k, \mathbf{Z}^k, \Lambda^k)\}$ is a sequence generated by Algorithm 1. Then it converges to a stationary point of [\(6\)](#).

Proof. First, notice that

$$\begin{aligned} & \mathcal{L}_\beta(\mathbf{L}^{k+1}, \mathbf{S}^{k+1}, \mathbf{Z}^{k+1}, \Lambda^{k+1}) - \mathcal{L}_\beta(\mathbf{L}^{k+1}, \mathbf{S}^{k+1}, \mathbf{Z}^{k+1}, \Lambda^k) \\ &= -\langle \Lambda^{k+1} - \Lambda^k, \mathbf{Z}^{k+1} - \mathbf{L}^{k+1} - \mathbf{S}^{k+1} \rangle = \frac{1}{\beta} \|\Lambda^{k+1} - \Lambda^k\|_F^2, \end{aligned}$$

where the second equality follows from (d). We then analyze the upper bound for $\frac{1}{\beta} \|\Lambda^{k+1} - \Lambda^k\|_F^2$. From (c), we have

$$\begin{aligned} 0 &= -\mathcal{E}^T(\mathbf{D} - \mathcal{E}(\mathbf{Z}^{k+1})) - \Lambda^k + \beta(\mathbf{Z}^{k+1} - \mathbf{L}^{k+1} - \mathbf{S}^{k+1}) \\ &= -\mathcal{E}^T(\mathbf{D} - \mathcal{E}(\mathbf{Z}^{k+1})) - \Lambda^{k+1}, \end{aligned}$$

where the last equality also follows from (d), and it can be transformed to

$$\Lambda^{k+1} = -\mathcal{E}^T(\mathbf{D} - \mathcal{E}(\mathbf{Z}^{k+1})).$$

Hence, for $k > 1$,

$$\Lambda^{k+1} - \mathbf{W}^k = -\mathcal{E}^T(\mathbf{D} - \mathcal{E}(\mathbf{Z}^{k+1})) + \mathcal{E}^T(\mathbf{D} - \mathcal{E}(\mathbf{Z}^k)) = \mathcal{E}^T \mathcal{E}(\mathbf{Z}^{k+1} - \mathbf{Z}^k).$$

It then follows that

$$\|\Lambda^{k+1} - \Lambda^k\|_F^2 \leq \lambda_{\max}^2 \|\mathbf{Z}^{k+1} - \mathbf{Z}^k\|_F^2,$$

where λ_{\max} is the largest eigenvalue of $\mathcal{E}^T \mathcal{E}$.

Next, note that $\mathcal{L}_\beta(\mathbf{L}^{k+1}, \mathbf{S}^{k+1}, \mathbf{Z}^{k+1}, \Lambda^k)$ is strongly convex (w.r.t. \mathbf{Z}) with modulus at least $\frac{\lambda_{\min} + \beta}{2}$, where λ_{\min} is smallest eigenvalue of $\mathcal{E}^T \mathcal{E}$. Using this fact and the definition of \mathbf{Z}^{k+1} , we see that

$$\begin{aligned} \mathcal{L}_\beta(\mathbf{L}^{k+1}, \mathbf{S}^{k+1}, \mathbf{Z}^{k+1}, \Lambda^k) - \mathcal{L}_\beta(\mathbf{L}^{k+1}, \mathbf{S}^{k+1}, \mathbf{Z}^k, \Lambda^k) \\ \leq -\frac{\lambda_{\min} + \beta}{2} \|\mathbf{Z}^{k+1} - \mathbf{Z}^k\|_F^2. \end{aligned}$$

Then, because \mathbf{S}^{k+1} is a minimizer of \mathbf{S} -subproblem with manifold \mathcal{M}_2 , we have

$$\mathcal{L}_\beta(\mathbf{L}^{k+1}, \mathbf{S}^{k+1}, \mathbf{Z}^k, \Lambda^k) - \mathcal{L}_\beta(\mathbf{L}^{k+1}, \mathbf{S}^k, \mathbf{Z}^k, \Lambda^k) \leq 0.$$

Similarly, \mathbf{L}^{k+1} is a minimizer of \mathbf{L} -subproblem, then we obtain

$$\mathcal{L}_\beta(\mathbf{L}^{k+1}, \mathbf{S}^k, \mathbf{Z}^k, \Lambda^k) - \mathcal{L}_\beta(\mathbf{L}^k, \mathbf{S}^k, \mathbf{Z}^k, \Lambda^k) \leq 0.$$

Finally, Summing the above inequalities, we can easily get

$$\begin{aligned} \mathcal{L}_\beta(\mathbf{L}^{k+1}, \mathbf{S}^{k+1}, \mathbf{Z}^{k+1}, \Lambda^{k+1}) - \mathcal{L}_\beta(\mathbf{L}^k, \mathbf{S}^k, \mathbf{Z}^k, \Lambda^k) \\ \leq \left(\frac{\lambda_{\max}^2}{\beta} - \frac{\lambda_{\min} + \beta}{2} \right) \|\mathbf{Z}^{k+1} - \mathbf{Z}^k\|_F^2. \end{aligned}$$

Thus, if $\frac{\lambda_{\max}^2}{\beta} - \frac{\lambda_{\min} + \beta}{2} \leq 0$, then the generated sequence $\{\mathcal{L}_\beta(\mathbf{L}^k, \mathbf{S}^k, \mathbf{Z}^k, \Lambda^k)\}_{k=1}^\infty$ is decreasing. According to [32], it is not hard to conclude that the sequence $\{(\mathbf{L}^k, \mathbf{D}^k, \mathbf{Z}^k, \Lambda^k)\}$ converges to a stationary point of problem (6). This completes the proof. \square

4. MCJSL for image denoising

In this section, the proposed MCJSL is applied to image denoising, where the images are added the Gaussian noise via different degrees. Meanwhile, some excellent methods such as BM3D [33], LSSC [34], NCSR [35], SAIST [36], WNNM [14] and ManiDec [25] are compared.

For a local patch \mathbf{y}_j in noisy image \mathbf{Y} , we can search for its non-local similar patches across a relatively large area around it by methods such as manifold projection. By stacking those nonlocal similar patches into a matrix, denoted by \mathbf{D}_j , we have $\mathbf{Y}_j = \mathbf{D}_j + \mathbf{E}_j$, where $\mathbf{D}_j = \mathbf{L}_j + \mathbf{S}_j$, \mathbf{L}_j and \mathbf{S}_j are the low-rank matrix and sparse matrix, and \mathbf{E}_j is the corresponding corruption matrix, respectively. Intuitively, the low-rank matrix approximation methods can be used to estimate \mathbf{D}_j from \mathbf{Y}_j . By aggregating all the estimated patches \mathbf{D}_j , the whole image can be reconstructed from its neighbors by minimizing the reconstruction error. We apply the proposed MADMM-based algorithm to each \mathbf{Y}_j to estimate \mathbf{L}_j and

\mathbf{S}_j for image denoising. By applying the above procedures to each patch and aggregating all patches together, the image \mathbf{D} can be reconstructed. In practice, we can run several iterations of this reconstruction process across all image patches to enhance the denoising outputs. The whole denoising algorithm is summarized in Algorithm 2.

Algorithm 2: Image Denoising by MCJSL (6)

Input: Noisy image \mathbf{Y} ;
Output: Denoised image $\widehat{\mathbf{D}}^k$;
Initialize: Primal variables $\widehat{\mathbf{D}}^{(0)} = \mathbf{Y}$ and $\widehat{\mathbf{Y}}^{(0)} = \mathbf{Y}$;
for $k = 1 : K$ **do**
 Iterative regularization
 $\widehat{\mathbf{Y}}^{(k)} = \widehat{\mathbf{L}}^{(k-1)} + \widehat{\mathbf{S}}^{(k-1)} + \delta(\mathbf{Y} - \widehat{\mathbf{Y}}^{(k-1)})$;
 for each patch \mathbf{L}_i and \mathbf{S}_i in $\widehat{\mathbf{L}}^{(k)}$ and $\widehat{\mathbf{S}}^{(k)}$ **do**
 Find similar patch group \mathbf{D}_i ;
 Apply the MADMM-based algorithm to estimate \mathbf{L}_i and \mathbf{S}_i ;
 End for
 Aggregate \mathbf{D}_j to form the clean image $\widehat{\mathbf{D}}^{(k)}$;
End for

4.1. Experimental setting

By comparing different image denoising approaches on 20 benchmark test images, which are shown in Fig. 2. The size of the first 12 images are 256×256 , and the remaining 8 images are 512×512 . Four different levels of additive white Gaussian noise, ranging from mean square error (MSE) $\sigma_n = 10$ to MSE $\sigma_n = 100$ are added, which imitate the real noise distribution as much as possible, but still have a certain distance with the real noise image. Therefore, it is still a challenge to establish a denoising approach in accordance with the real noise distribution.

In our experiments, the chosen patch numbers range from 70 to 140 for $\sigma_n \leq 20$, $20 < \sigma_n \leq 40$, $40 < \sigma_n \leq 60$ and $60 < \sigma_n$, respectively. At these noisy levels, the iterative regularization δ is set as 0.1, the minimum of iteration times K is fixed to 4, 6, 8, and 8, and patch sizes are 6×6 , 7×7 , 8×8 , 9×9 , respectively. Besides, the parameters λ_1, λ_2 are determined by the 5-fold cross-validation technique. The maximum number of iterations is set as 500, and the stopping criterion is defined as

$$\text{RelErr} = \max \left\{ \frac{\|\mathbf{L}^{k+1} - \mathbf{L}^k\|_F}{\|\mathbf{L}^k\|_F + 1}, \frac{\|\mathbf{S}^{k+1} - \mathbf{S}^k\|_F}{\|\mathbf{S}^k\|_F + 1} \right\}$$

with RelErr being 10^{-3} .

4.2. Experimental results

Under the influence of these noise levels, the denoising results in terms of peak signal-to-noise ratio (PSNR) and structural similarity (SSIM) are listed in Table 1 and Table 2. Moreover, the average results on different noisy levels are shown in Table 3. It can be observed that the proposed MCJSL accomplishes the highest SSIM and PSNR among almost all approaches. Although the ManiDec method also employs the manifold constraint and sparsity approach, it does not achieve the best results. In comparison with ManiDec, the proposed MCJSL achieves from 0.03 dB to 0.17 dB improvement on average. Meanwhile, the SSIM values of MCJSL are higher than ManiDec. This improvement is noteworthy since few methods can exceed BM3D by an average of more than 0.4 dB [37]. The visual quality of comparison results of denoised



Fig. 2. The 20 test images employed in image denoising experiments.

images can be observed in [Figs. 3 and 4](#). It is easy to see that: 1) NNM, EPLL, and LSSC can not effectively suppress the added noises because the texture details of the mast are lost. 2) NCSR and SAIST over smooth texture details, which leads to the blurring of the overall effect of the image. 3) BM3D, WNNM, and ManiDec guarantee the smoothness of the image, while some artifacts appear and the edge structures of the object are not well preserved. 4) The proposed MCJSL can preserve the edge of the target while denoising, and the PSNR and SSIM value shows the superiority of our method.

Next, the evaluated results on the real-world noisy images are displayed in [Figs. 5 and 6](#), which is not a simple Gaussian distribution, and may be Poisson, Salt & Pepper or other mixture of multiple noises. Therefore, it is still a challenge to remove all kinds of noise through data denoising approach. The classical method [38] is adopted to estimate the noise level, and the estimated noise level was utilized for all the competing methods. Compared with the ordinary image, the real image has abundant texture information, clear content, clear and easy to read, which fully shows the double advantages of the image. The comparison results demonstrate that the proposed MCJSL holds more local structures and obtains clearer texture after image denoising.

4.3. Elapsed time

We also present the elapsed time of different denoising methods to illustrate the superiority of the proposed MCJSL in the computation time. The experimental platform is a desktop computer with an Intel 3.6 GHz Intel Xeon W-2123 CPU and 32 GB of memory. The running times of various methods are shown in [Table 4](#). Some observations can be obtained as follow:

- Although BM3D achieves the smallest running time, the denoising performance is not excellent. In comparison to WNNM, the elapsed time of the proposed MCJSL is reduced by at least 18% on 20 test images. In particular, the running time is 27.7% less than that of WNNM when the noisy level $\sigma_n = 30$. This demon-

strates the effectiveness of manifold constrained joint sparse learning.

- Compared with ManiDec, the proposed MCJSL is still slightly faster. Nevertheless, the PSNR values have more than 0.1%~0.6% improvement in these 20 test images. Significantly, the SSIM values have 0.5% improvement when the noisy level $\sigma_n = 100$. The above experimental results prove the efficiency of MCJSL algorithm in the field of image denoising.

5. MCJSL for background subtraction

The purpose of SVD/PCA is to reduce the dimension of the data set while retaining as much information as possible. However, the sparsity of data will be higher with the increase of dimensions. It is more difficult to explore the same data set in high-dimensional vector space than in the same sparse data set. Especially in the traditional PCA algorithm, the measurement of the error depends on the L_2 norm fidelity to reduce the noise interference with sparse property. Therefore, the effect of image restoration depends on the complete and accurate representation of sparse noise results. To address these problems, various RPCA models are proposed to eliminate data with high amplitude sharp noise. The NNM-RPCA model in [9], WNNM-RPCA model in [14] and ManiDec [25] present efficient sparse data separation solutions by ADMM. In this paper, the MCJSL approach is proposed to change the conditions of comparison during the iteration in WNNM-RPCA and ManiDec.

Next, we design a comprehensive simulation to compare the performance of MCJSL, ManiDec and WNNM-RPCA, and then compare the above methods with the typical low-rank learning method designed to demonstrate the superiority of the MCJSL method in background subtraction.

5.1. Experimental results on generated data

To assess the performance of the presented MCJSL model, the quantitative synthetic low-rank matrix restoring simulations are

Table 1

Denoising results (PSNR, dB) on test images.

	$\sigma_n = 10$								$\sigma_n = 30$										
	NNM	BM3D	EPLL	LSSC	NCSR	SAIST	WNNM	ManiDec	MCJSL	NNM	BM3D	EPLL	LSSC	NCSR	SAIST	WNNM	ManiDec	MCJSL	
C.Man	32.87	34.18	34.02	34.24	34.18	34.30	34.44	34.46	34.50	27.43	28.64	28.36	28.63	28.59	28.36	28.80	28.84	28.88	
House	35.97	36.71	35.75	36.95	36.80	36.66	36.95	36.99	37.05	30.99	32.09	31.23	32.41	32.07	32.30	32.52	32.53	32.60	
Peppers	33.77	34.68	34.54	34.80	34.68	34.82	34.95	34.98	35.03	28.11	29.28	29.16	29.25	29.10	29.24	29.49	29.52	29.57	
Montage	36.09	37.35	36.49	37.26	37.17	37.46	37.84	37.87	37.94	29.28	31.38	30.17	31.10	30.92	31.06	31.65	31.69	31.84	
Leaves	33.55	34.04	33.29	34.52	34.53	34.92	35.20	35.25	35.32	26.81	27.81	27.65	27.52	27.70	27.78	27.92	28.08	28.30	28.70
StarFish	32.62	33.30	32.29	33.74	33.65	33.72	33.99	34.01	34.10	26.62	27.65	27.52	27.70	27.78	27.92	28.08	28.30	28.98	
Monarch	33.54	34.12	34.27	34.44	34.51	34.76	35.03	35.07	35.13	27.44	28.36	28.35	28.20	28.46	28.65	28.92	28.98	29.05	
Airplane	32.19	33.33	33.39	33.51	33.40	33.43	33.64	33.67	33.72	26.53	27.56	27.67	27.53	27.66	27.83	27.86	27.91		
Paint	33.13	34.00	34.01	34.35	34.15	34.28	34.50	34.53	34.61	27.02	28.29	28.33	28.29	28.10	28.44	28.58	28.60	28.65	
J.Bean	37.52	37.91	37.63	38.69	38.31	38.37	38.93	38.98	39.25	31.03	31.97	31.56	32.39	32.13	32.14	32.46	32.55	32.78	
Fence	32.62	33.50	32.89	33.60	33.65	33.76	33.93	33.96	34.01	27.19	28.19	27.23	28.16	28.23	28.26	28.56	28.59	28.63	
Parrot	32.54	33.57	33.58	33.62	33.56	33.66	33.81	33.85	33.91	27.26	28.12	28.07	27.99	28.07	28.12	28.33	28.35	28.38	
Lena	35.19	35.93	35.58	35.83	35.85	35.90	36.03	36.05	36.10	30.15	31.26	30.79	31.18	31.06	31.27	31.43	31.47	31.52	
Barbara	34.40	34.98	33.61	34.98	35.00	35.24	35.51	35.54	35.61	28.59	29.81	27.57	29.60	29.62	30.14	30.31	30.35	30.41	
Boat	33.05	33.92	33.66	34.01	33.91	33.91	34.09	34.13	34.16	27.82	29.12	28.89	29.06	28.94	28.98	29.24	29.27	29.32	
Hill	32.89	33.62	33.48	33.66	33.69	33.65	33.79	33.82	33.86	28.11	29.16	28.90	29.09	28.97	29.06	29.25	29.28	29.31	
F.print	31.38	32.46	32.12	32.57	32.68	32.69	32.82	32.84	32.86	25.84	26.83	26.19	26.68	26.92	26.95	26.99	27.02	27.12	
Man	32.99	33.98	33.97	34.10	34.05	34.12	34.23	34.27	36.34	27.87	28.86	28.83	28.87	28.78	28.81	29.00	29.03	29.08	
Couple	32.97	34.04	33.85	34.01	34.00	33.96	34.14	34.17	34.21	27.36	28.87	28.62	28.77	8.57	28.72	28.98	29.00	29.02	
Straw	29.84	30.89	30.74	31.25	31.35	31.49	31.62	31.67	31.74	23.52	24.84	24.64	24.99	25.00	25.23	25.27	25.33	25.50	
AVE.	33.462	34.326	34.008	34.507	34.456	34.555	34.772	34.806	34.973	27.753	28.905	28.463	28.877	28.849	28.980	29.214	29.260	29.363	
$\sigma_n = 50$								$\sigma_n = 100$											
	NNM	BM3D	EPLL	LSSC	NCSR	SAIST	WNNM	ManiDec	MCJSL	NNM	BM3D	EPLL	LSSC	NCSR	SAIST	WNNM	ManiDec	MCJSL	
C.Man	24.88	26.12	26.02	26.35	26.14	26.15	26.42	26.46	26.53	21.49	23.07	22.86	23.15	22.93	23.09	23.36	23.38	23.44	
House	27.84	29.69	28.76	29.99	29.62	30.17	30.32	30.35	30.41	23.65	25.87	25.19	25.71	25.56	26.53	26.68	26.73	26.88	
Peppers	25.29	26.68	26.63	26.79	26.82	26.73	26.91	26.95	27.04	21.24	23.39	23.08	23.20	22.84	23.32	23.46	23.51	23.65	
Montage	26.04	27.9	27.17	28.10	27.84	28.00	28.27	28.32	28.57	21.70	23.89	23.42	23.77	23.74	23.98	24.16	24.18	24.25	
Leaves	23.36	24.68	24.38	24.81	25.04	25.25	25.47	25.51	25.62	18.73	20.91	20.25	20.58	20.86	21.40	21.57	21.62	21.79	
StarFish	23.83	25.04	25.04	25.12	25.07	25.29	25.44	25.47	25.54	20.58	22.10	21.92	21.77	21.91	22.10	22.22	22.24	22.31	
Monarch	24.46	25.82	25.78	25.88	25.73	26.10	26.32	26.36	26.43	20.22	22.52	22.23	22.24	22.11	22.61	22.91	23.95	23.12	
Airplane	23.97	25.10	25.24	25.25	24.93	25.34	25.43	25.46	25.51	20.73	22.11	22.02	21.69	21.83	22.27	22.55	22.57	22.63	
Paint	24.19	25.67	25.77	25.59	25.37	25.77	25.98	25.98	26.02	21.02	22.51	22.50	22.14	22.11	22.42	22.74	22.75	22.79	
J.Bean	27.96	29.26	28.75	29.42	29.29	29.32	29.62	29.71	29.89	23.79	25.80	25.17	25.64	25.66	25.82	26.04	26.12	26.22	
Fence	24.59	25.92	24.58	25.87	25.78	26.00	26.43	26.44	26.49	21.23	22.92	21.11	22.71	22.23	22.98	23.37	23.38	23.44	
Parrot	24.87	25.90	25.84	25.82	25.71	25.95	26.09	26.11	26.14	21.38	22.96	22.71	22.79	22.53	23.04	23.19	23.20	23.25	
Lena	27.74	29.05	28.42	28.95	28.90	29.01	29.24	29.25	29.28	24.41	25.95	25.30	25.96	25.71	25.93	26.20	26.22	26.28	
Barbara	25.75	27.23	24.82	27.03	26.99	27.51	27.79	27.81	27.86	22.14	23.62	22.14	23.54	23.20	24.07	24.37	24.37	24.43	
Boat	25.39	26.78	26.65	26.77	26.66	26.63	26.97	26.98	27.01	22.48	23.97	23.71	23.87	23.68	23.80	24.10	24.11	24.14	
Hill	25.94	27.19	26.96	27.14	26.99	27.04	27.34	27.35	27.39	23.32	24.58	24.43	24.47	24.36	24.29	24.75	24.78	24.82	
F.print	23.37	24.53	23.59	24.26	24.48	24.52	24.67	24.71	24.80	20.01	21.61	19.85	21.30	21.39	21.62	21.81	21.84	21.90	
Man	25.66	26.81	26.72	26.72	26.67	26.68	26.94	26.95	26.99	22.88	24.22	24.07	23.98	24.02	24.01	24.36	24.37	24.42	
Couple	24.84	26.46	26.24	26.35	26.19	26.30	26.65	26.65	26.69	22.07	23.51	23.32	23.27	23.15	23.21	23.55	23.55	23.61	
Straw	20.99	22.29	21.93	22.51	22.30	22.65	22.74	22.78	22.99	18.33	19.43	18.84	19.43	19.10	19.42	19.67	20.05	20.12	
AVE.	25.048	26.406	25.965	26.436	26.326	26.521	26.752	26.780	26.860	21.570	23.247	22.706	23.061	22.996	23.296	23.555	23.646	23.675	

Table 2

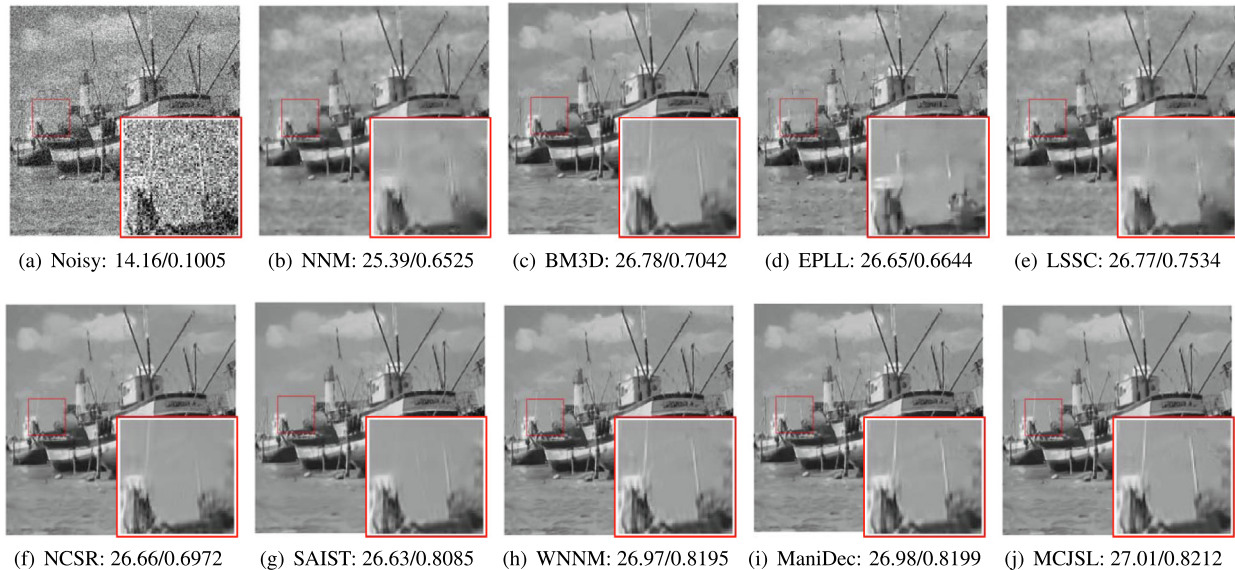
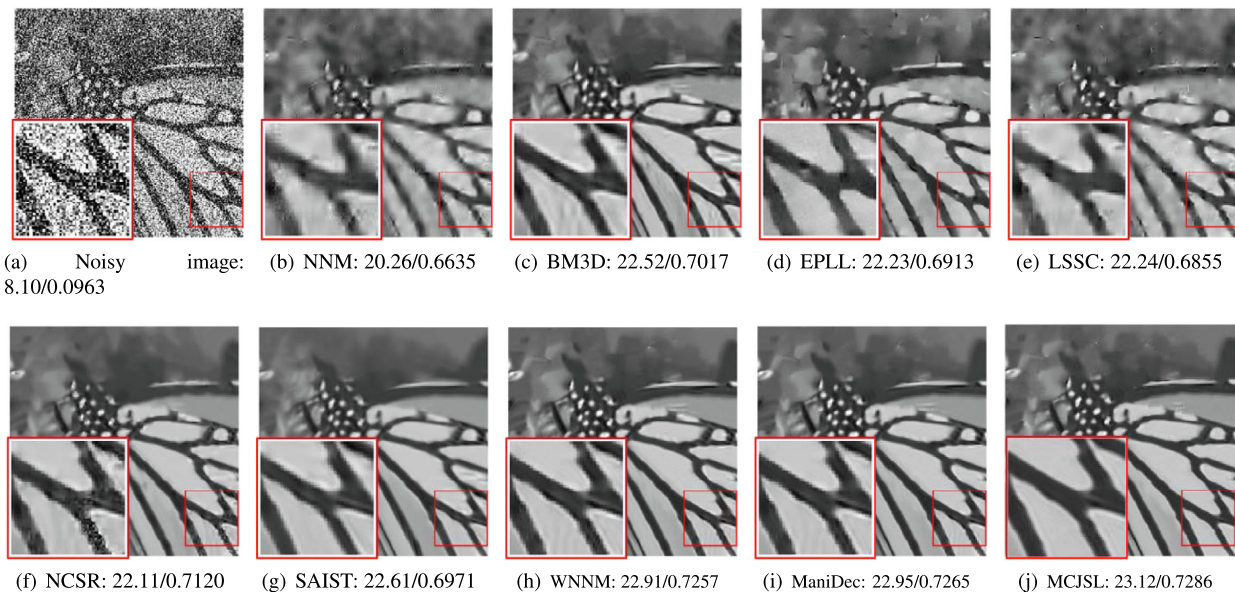
Denoising results (SSIM) on test images.

	$\sigma_n = 10$								$\sigma_n = 30$									
	NNM	BM3D	EPLL	LSSC	NCSR	SAIST	WNNM	ManiDec	MCJSL	NNM	BM3D	EPLL	LSSC	NCSR	SAIST	WNNM	ManiDec	MCJSL
C.Man	0.9128	0.9300	0.9289	0.9302	0.9312	0.9312	0.9326	0.9335	0.9343	0.8022	0.8308	0.8121	0.8245	0.8392	0.8135	0.8399	0.8402	0.8406
House	0.9018	0.9234	0.9032	0.9189	0.9238	0.9164	0.9228	0.9231	0.9219	0.8321	0.8500	0.8338	0.8469	0.8486	0.8499	0.8523	0.8529	0.8536
Peppers	0.9144	0.9303	0.9274	0.9275	0.9271	0.9282	0.9300	0.9304	0.9303	0.8416	0.8528	0.8467	0.8521	0.8501	0.8445	0.8567	0.8567	0.8569
Montage	0.9589	0.9665	0.9636	0.9655	0.9676	0.9672	0.9694	0.9695	0.9692	0.9052	0.9083	0.8961	0.9064	0.9176	0.9099	0.9197	0.9195	0.9186
Leaves	0.9676	0.9775	0.9752	0.9799	0.9807	0.9807	0.9835	0.9836	0.9834	0.9089	0.9254	0.9196	0.9296	0.9324	0.9245	0.9389	0.9382	0.9385
StarFish	0.9215	0.9280	0.9234	0.9325	0.9347	0.9353	0.9373	0.9372	0.9372	0.8156	0.8217	0.8058	0.8265	0.8306	0.8248	0.8357	0.8362	0.8371
Monarch	0.9544	0.9549	0.9569	0.9546	0.9572	0.9555	0.9603	0.9604	0.9603	0.8665	0.8808	0.8792	0.8867	0.8855	0.8789	0.8926	0.8930	0.8937
Airplane	0.9215	0.9276	0.9231	0.9245	0.9253	0.9277	0.9273	0.9275	0.9281	0.8237	0.8419	0.8357	0.8234	0.8394	0.8438	0.8442	0.8459	
Paint	0.9199	0.9297	0.9260	0.9314	0.9311	0.9320	0.9351	0.9351	0.9352	0.8110	0.8256	0.8110	0.8201	0.8214	0.8267	0.8333	0.8336	0.8340
J.Bean	0.9713	0.9794	0.9834	0.9788	0.9813	0.9775	0.9831	0.9830	0.9831	0.8035	0.9371	0.9483	0.9313	0.9453	0.9240	0.9438	0.9441	0.9455
Fence	0.9156	0.9358	0.9330	0.9326	0.9380	0.9332	0.9404	0.9408	0.9415	0.8120	0.8293	0.8028	0.8269	0.8303	0.8150	0.8381	0.8362	0.8365
Parrot	0.9100	0.9282	0.9212	0.9212	0.9281	0.9304	0.9281	0.9289	0.9297	0.8046	0.8358	0.8214	0.8262	0.8318	0.8295	0.8346	0.8352	0.8365
Lena	0.9058	0.9165	0.9134	0.9435	0.9157	0.9666	0.9694	0.9693	0.9694	0.8744	0.8456	0.8386	0.8465	0.8456	0.9018	0.9174	0.9174	0.9176
Barbara	0.9186	0.9412	0.9382	0.9548	0.9416	0.9712	0.9774	0.9772	0.9773	0.8673	0.8673	0.8518	0.8625	0.8671	0.8877	0.9343	0.9342	0.9341
Boat	0.9056	0.8877	0.8790	0.9305	0.8883	0.9656	0.9675	0.9674	0.9675	0.7262	0.7782	0.7470	0.7835	0.7714	0.8824	0.8876	0.8878	0.8882
Hill	0.8745	0.8835	0.8751	0.9327	0.8863	0.9578	0.9588	0.9596	0.9599	0.7343	0.7507	0.7161	0.7497	0.7428	0.8588	0.8626	0.8629	0.8635
F.print	0.9588	0.9678	0.9657	0.9856	0.9700	0.9901	0.9907	0.9906	0.9907	0.8845	0.8900	0.8732	0.8922	0.8941	0.9449	0.9501	0.9518	0.9526
Man	0.8859	0.9074	0.9015	0.9438	0.9083	0.9644	0.9649	0.9651	0.9653	0.7447	0.7795	0.7510	0.7791	0.7779	0.8735	0.8745	0.8765	0.8775
Couple	0.9025	0.9084	0.8964	0.9396	0.9084	0.9661	0.9674	0.9670	0.9675	0.7652	0.7932	0.7535	0.7911	0.7827	0.8812	0.8903	0.8906	0.8914
Straw	0.9512	0.9605	0.9596	0.9782	0.9643	0.9862	0.9878	0.9876	0.9878	0.8210	0.8323	0.8125	0.8372	0.9163	0.9277	0.9281	0.9290	0.9290
AVE.	0.9236	0.9342	0.9297	0.9453	0.9354	0.9542	0.9567	0.9568	0.9570	0.8202	0.8438	0.8278	0.8418	0.8446	0.8714	0.8837	0.8840	0.8846
	$\sigma_n = 50$								$\sigma_n = 100$									
	NNM	BM3D	EPLL	LSSC	NCSR	SAIST	WNNM	ManiDec	MCJSL	NNM	BM3D	EPLL	LSSC	NCSR	SAIST	WNNM	ManiDec	MCJSL
C.Man	0.7542	0.7764	0.7617	0.7685	0.7834	0.7664	0.7848	0.7856	0.7872	0.6215	0.6880	0.6351	0.6654	0.7059	0.6768	0.6968	0.6971	0.6975
House	0.7789	0.8146	0.7845	0.8159	0.8161	0.8186	0.8231	0.8239	0.8254	0.6754	0.7229	0.6695	0.7269	0.7407	0.7402	0.7563	0.7580	0.7599
Peppers	0.7815	0.7939	0.7832	0.7802	0.7988	0.7872	0.8008	0.8020	0.8032	0.6248	0.6832	0.6653	0.6836	0.7053	0.6962	0.6978	0.6989	0.7105
Montage	0.8652	0.8580	0.8342	0.8590	0.8785	0.8660	0.8752	0.8753	0.8755	0.6978	0.7441	0.7075	0.7256	0.7958	0.7721	0.7768	0.7792	0.7847
Leaves	0.8475	0.8638	0.8636	0.8642	0.8793	0.8653	0.8925	0.8924	0.8925	0.7063	0.7423	0.7161	0.7095	0.7622	0.7822	0.7884	0.7899	0.7950
StarFish	0.7153	0.7377	0.7200	0.7316	0.7452	0.7392	0.7596	0.7596	0.7597	0.5806	0.6014	0.5578	0.6025	0.6067	0.6099	0.6170	0.6186	0.6204
Monarch	0.8098	0.8197	0.8172	0.8046	0.8259	0.8124	0.8350	0.8352	0.8354	0.6635	0.7017	0.6913	0.6855	0.7120	0.6971	0.7257	0.7265	0.7286
Airplane	0.7596	0.7784	0.7695	0.7586	0.7746	0.7670	0.7850	0.7836	0.7839	0.6098	0.6654	0.6409	0.6635	0.6814	0.6588	0.6854	0.6853	0.6854
Paint	0.7201	0.7428	0.7211	0.7451	0.7349	0.7437	0.7537	0.7546	0.7548	0.5821	0.6037	0.5595	0.5968	0.5985	0.5892	0.6168	0.6183	0.6200
J.Bean	0.8834	0.9038	0.9163	0.8631	0.9143	0.8677	0.9098	0.9122	0.9141	0.7564	0.8226	0.8420	0.8126	0.8475	0.7929	0.8337	0.8342	0.8454
Fence	0.7196	0.7598	0.7198	0.7119	0.7476	0.7162	0.7777	0.7768	0.7766	0.5231	0.6354	0.5751	0.6011	0.5998	0.6052	0.6501	0.6523	0.6533
Parrot	0.7532	0.7868	0.7709	0.7566	0.7806	0.7655	0.7847	0.7852	0.7862	0.6214	0.6957	0.6831	0.6959	0.7002	0.6989	0.7045	0.7064	0.7089
Lena	0.8001	0.8007	0.7936	0.8321	0.8035	0.8431	0.8752	0.8756	0.8762	0.6987	0.7109	0.7131	0.7045	0.7276	0.7328	0.7896	0.7908	0.7924
Barbara	0.7425	0.7932	0.7635	0.8056	0.7891	0.8044	0.8884	0.8880	0.8881	0.5864	0.6417	0.6096	0.7025	0.6389	0.6702	0.7739	0.7729	0.7732
Boat	0.6525	0.7042	0.6644	0.7534	0.6972	0.8085	0.8195	0.8199	0.8212	0.5521	0.6723	0.5558	0.6201	0.5929	0.6713	0.6926	0.6934	0.6947
Hill	0.6355	0.6757	0.6346	0.7689	0.6617	0.7811	0.7906	0.7908	0.7909	0.5067	0.6469	0.5262	0.5698	0.5604	0.6445	0.6599	0.6602	0.6610
F.print	0.6214	0.8258	0.7946	0.8801	0.8214	0.8831	0.9054	0.9074	0.9104	0.6059	0.7036	0.6205	0.7124	0.6826	0.6774	0.7961	0.7992	0.8039
Man	0.6549	0.7047	0.6695	0.7864	0.6996	0.7976	0.8035	0.8040	0.8054	0.6136	0.6375	0.5649	0.6602	0.6016	0.6667	0.6834	0.6836	0.6836
Couple	0.6846	0.7059	0.6567	0.7964	0.6939	0.8010	0.8206	0.8200	0.8201	0.5215	0.5669	0.5059	0.5723	0.5563	0.6425	0.6612	0.6625	0.6630
Straw	0.6219	0.6905	0.6632	0.8106	0.6875	0.7995	0.8468	0.8488	0.8524	0.3345	0.4249	0.2546	0.5001	0.3694	0.4692	0.5907	0.6122	0.6364
AVE.	0.7401	0.7768	0.7551	0.7946	0.7767	0.8017	0.8266	0.8270	0.8280	0.6041	0.6605	0.6147	0.6593	0.6747	0.7098	0.7120	0.7159	0.7159

Table 3

The average PSNR(dB) and SSIM values on test images.

	$\sigma_n = 10$	$\sigma_n = 20$	$\sigma_n = 30$	$\sigma_n = 40$	$\sigma_n = 50$	$\sigma_n = 75$	$\sigma_n = 100$
NNM	33.462/0.9236	30.040/0.8665	27.753/0.8202	26.422/0.7836	25.048/0.7401	22.204/0.7096	21.570/0.6041
BM3D	34.326/0.9342	30.840/0.8842	28.905/0.8438	27.360/0.8046	26.406/0.7768	24.560/0.7108	23.247/0.6655
EPLL	34.008/0.9532	30.470/0.8766	28.463/0.8278	27.060/0.7934	25.965/0.7551	24.020/0.6830	22.706/0.6147
LSSC	34.507/0.9453	30.950/0.9044	28.877/0.8418	27.500/0.8364	26.436/0.7946	24.450/0.7024	23.061/0.6605
NCSR	34.456/0.9354	30.890/0.8853	28.849/0.8446	27.390/0.8068	26.326/0.7767	24.340/0.7127	22.996/0.6593
SAIST	34.555/0.9309	30.970/0.9116	28.980/0.8714	27.590/0.8360	26.521/0.8017	24.620/0.7243	23.296/0.6747
WNNM	34.772/0.9567	31.200/0.9169	29.214/0.8837	27.780/0.8516	26.752/0.8266	24.860/0.7658	23.555/0.7098
ManiDec	34.806/0.9658	31.312/0.9170	29.331/0.8840	27.805/0.8522	26.780/0.8270	24.906/0.7669	23.646/0.7120
MCJSL	34.973/0.9570	31.422/0.9173	29.363/0.8846	27.852/0.8532	26.860/0.8280	24.950/0.7685	23.675/0.7159

**Fig. 3.** Denoising results PSNR(dB)/SSIM on image Boats under noisy level $\sigma_n = 50$. The demarcated area is enlarged in the right bottom corner for better visualization.**Fig. 4.** Denoising results PSNR(dB)/SSIM on image Monarch under noisy level $\sigma_n = 100$. The demarcated area is enlarged in the left bottom corner for better visualization.

generated for experimental testing. In our experiment, the noisy observation matrix $\mathbf{Y} = \mathbf{D} + \mathbf{E}$, where the ground truth matrix $\mathbf{D} = \mathbf{L}\mathbf{S}^T$, and sparse noise \mathbf{E} has $p_e \times k^2$ randomly distributed

non-zero terms with values between $[-5, 5]$. Here \mathbf{L} and \mathbf{S} obey the Gaussian distribution $\mathcal{N}(0, 1)$, and the size are both $k \times r$ where $r = p_r \times k$ constrains the upper bound of $\text{Rank}(\mathbf{D})$. For the parame-

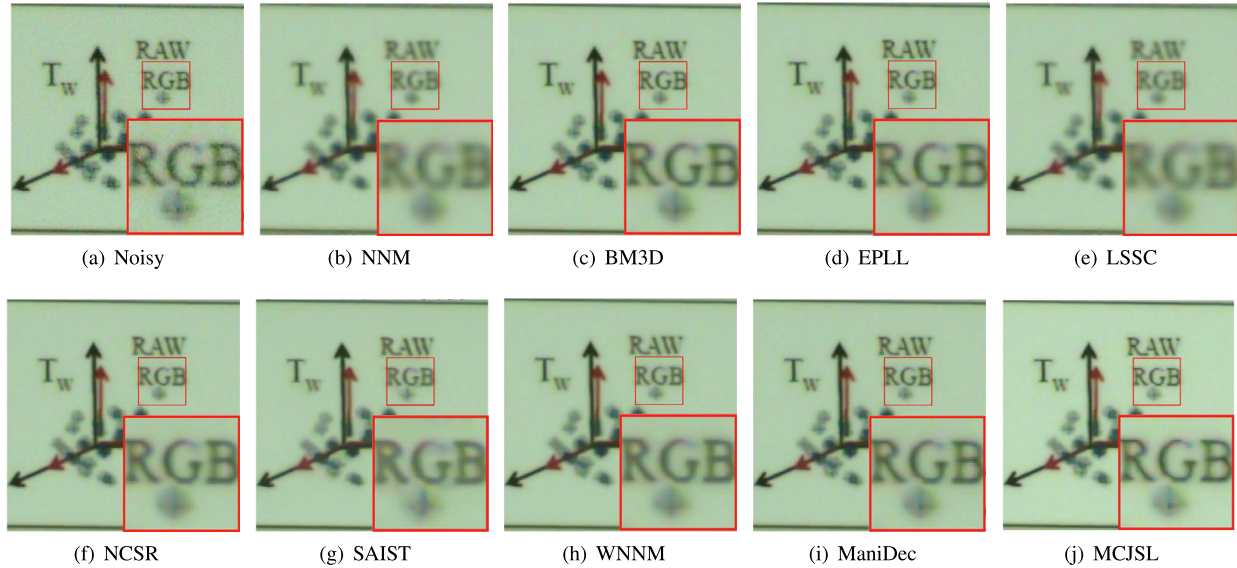


Fig. 5. Denoising results on a real "RGB" image.

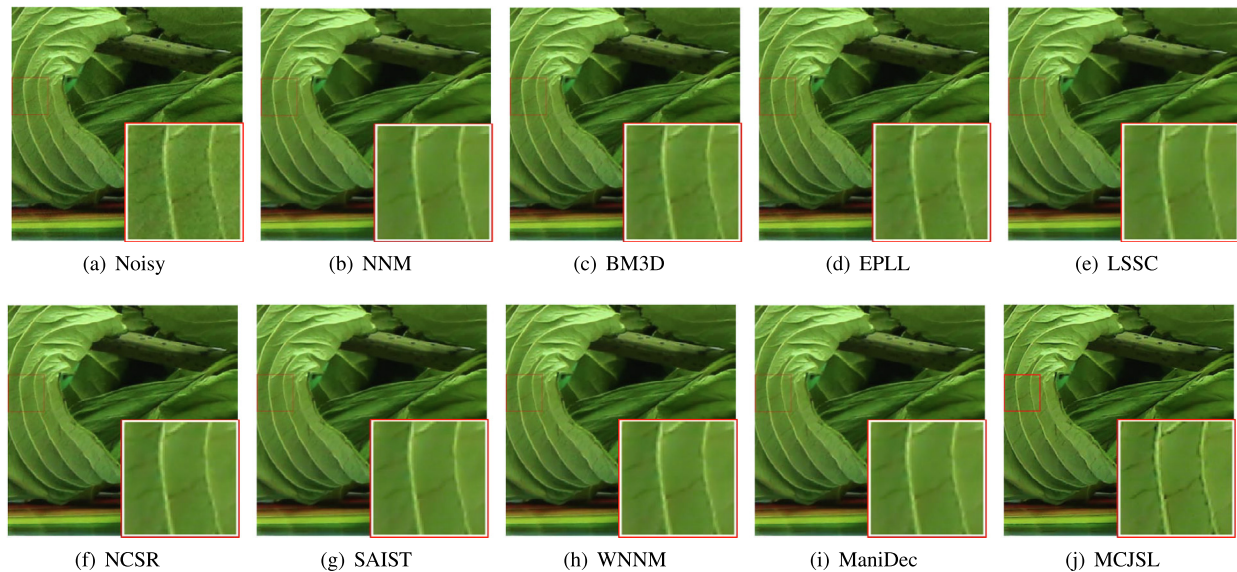


Fig. 6. Denoising results on a real "spinach" image.

Table 4

The average times (s) values on test images.

	$\sigma_n = 10$	$\sigma_n = 20$	$\sigma_n = 30$	$\sigma_n = 40$	$\sigma_n = 50$	$\sigma_n = 75$	$\sigma_n = 100$
NNM	118.145	156.114	160.027	289.284	199.176	211.140	211.756
BM3D	0.647	1.430	0.741	1.403	1.092	1.872	1.144
EPLL	75.201	74.113	75.025	76.076	74.891	75.554	76.230
LSSC	65.316	64.208	63.629	66.157	64.424	66.623	66.780
NCSR	287.101	358.123	350.018	838.055	705.036	430.101	412.025
SAIST	86.500	182.045	182.256	291.156	166.900	255.114	255.456
WNNM	127.060	134.405	264.150	268.056	216.960	329.693	328.200
ManiDec	110.112	119.508	210.050	224.115	180.076	279.369	269.113
MCJSL	97.075	110.086	191.925	211.752	168.595	253.071	251.550

ter k , set it to 400. For the parameters p_r and p_e , set it from 0.01 to 0.5 in steps of 0.01. The synthetic low-rank matrix is generated 10 times for each parameter $\{p_r, p_e\}$ setting, and the ultimate result is taken as the average of measurements of these 10 times. Following

the advised setting of [9,14], the parameter λ and in NNM-RPCA algorithm is empirically set as $1/\sqrt{k}$, and the parameter C in WNNM-RPCA algorithm equals the square root of the matrix size, in other words, set $C = \sqrt{k \times k} = k$ in our experiments. For Mani-

Dec and our MCJSL model, the parameter λ and C are set as the same value as before. It is worth noting that the parameters for both algorithms in ADMM are set as $\beta = 1.03$. For the convenience of comparison, representative experimental results are enumerated in Table 5. It is easy to observe that the NNM-RPCA, WNNM-RPCA, ManiDec and MCJSL models can accurately estimate the ground truth matrix when the rank of matrix or the number of corrupted terms is small. However, with the rank of matrix or the number of corrupted terms increasing larger, NNM-RPCA, WNNM-RPCA and ManiDec cannot accurately estimate the ground truth matrix. Regardless, in these cases, the error of the results by MCJSL is smallest compared with these their techniques including NNM-RPCA, WNNM-RPCA and ManiDec. With different values of $\{p_r, p_e\}$, the logarithmic scale relative error diagram of the recovered matrices by NNM-RPCA, WNNM-RPCA, ManiDec and MCJSL are shown

in Fig. 7, it can be observed that the successful area of MCJSL is largest among the four models, indicating that MCJSL has the best low-rank matrix reconstruction ability in the case of sparse/outliers noise. However, there are still some differences between synthetic low-rank recovering simulations data and real-world data in complex environment, so we will utilize the real datasets to verify the performance of our algorithm in the next subsection.

5.2. Experimental results on background removal

In this subsection, we will verify the superiority of the proposed MCJSL over state-of-the-art methods, such as MOG [39], FPCP [40], VBRPCA [41], DECOLOR [42,43], PRMF [44], GoDec [45], FW-T [46] WNNM [14], and ManiDec [25]. Besides, four benchmark datasets for background subtraction are considered, including I2R [47],

Table 5

Relative error of low-rank matrix recovery results by NNM-RPCA, WNNM-RPCA and ManiDec, with p_e fixed as 0.05, 0.1, 0.2, and p_r varying from 0.05 to 0.45 with step length 0.05

Rank(X)	20	40	60	80	100	120	140	160	180
$p_e = 0.05$									
NNM-RPCA	2.41e-8	3.57e-8	5.32e-8	7.91e-8	2.90e-4	1.72e-2	6.49e-2	0.13	0.21
WNNM-RPCA	1.79e-8	3.49e-8	5.83e-8	6.53e-8	9.28e-8	1.30e-7	1.68e-7	2.02e-7	2.43e-7
ManiDec	1.98e-8	3.44e-8	5.67e-8	6.54e-8	8.88e-8	1.21e-7	1.45e-7	1.85e-7	2.01e-7
MCJSL	2.06e-8	3.38e-8	5.11e-8	6.50e-8	8.36e-8	1.03e-8	1.21e-8	1.44e-8	1.81e-7
$p_e = 0.1$									
NNM-RPCA	2.26e-8	4.58e-8	7.44e-8	2.50e-4	2.31e-2	6.16e-2	9.96e-2	0.15	0.22
WNNM-RPCA	2.34e-8	3.71e-8	6.03e-8	8.87e-8	1.37e-7	1.82e-7	2.24e-7	4.80e-3	2.41e-2
ManiDec	2.14e-8	3.74e-8	5.88e-8	8.02e-8	1.01e-7	1.44e-7	2.01e-7	2.20e-3	2.39e-2
MCJSL	1.97e-8	3.70e-8	5.79e-8	6.90e-8	9.18e-8	1.11e-7	1.36e-7	1.69e-7	2.31e-7
$p_e = 0.2$									
NNM-RPCA	4.22e-8	6.84e-8	8.89e-3	5.80e-2	9.29e-2	0.12	0.14	0.18	0.24
WNNM-RPCA	3.68e-8	6.09e-8	1.18e-7	1.72e-7	3.76e-4	2.94e-2	5.42e-2	6.82e-2	7.53e-2
ManiDec	3.60e-8	5.84e-8	8.01e-8	1.45e-7	3.33e-4	2.42e-2	5.31e-2	6.36e-2	7.21e-2
MCJSL	3.56e-8	5.19e-8	5.39e-8	7.13e-8	9.73e-8	1.44e-7	5.13e-2	6.10e-2	6.90e-2

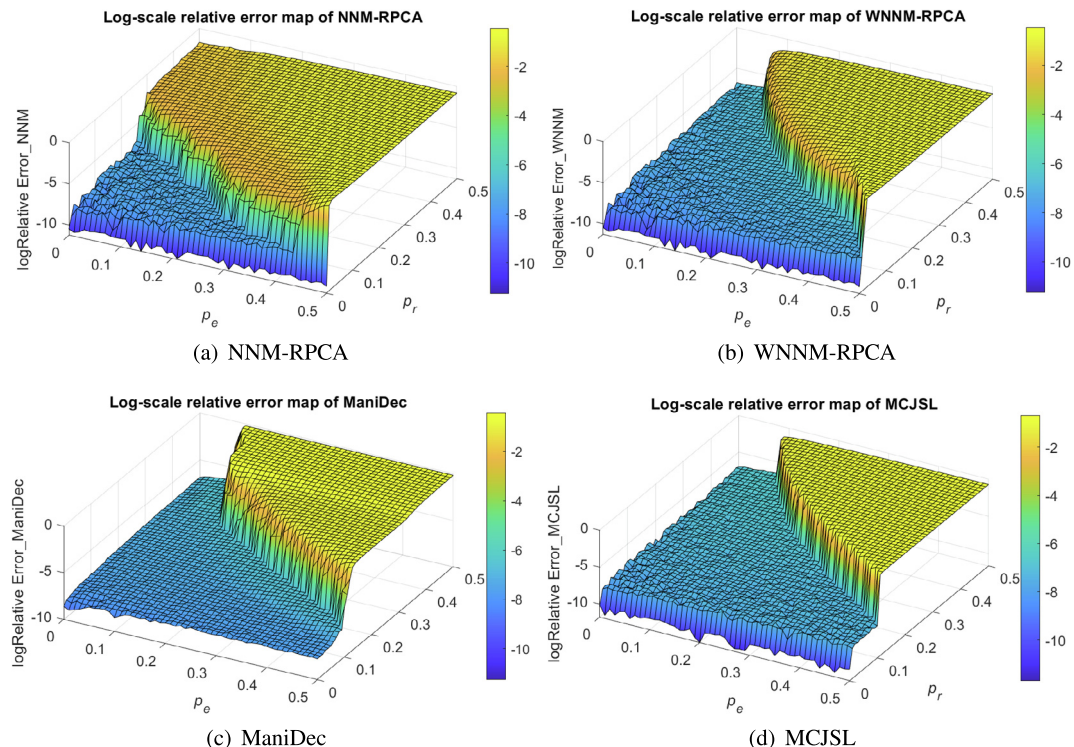


Fig. 7. The log-scale relative error $\log \frac{\|D - \hat{D}\|_F}{\|D\|_F}$ of NNM-RPCA, WNNM-RPCA, ManiDec and MCJSL with different rank and outlier rate settings $\{p_e, p_r\}$.

UCSD [48], CDnet [49] and LASIESTA [50]. I2R contains nine videos (with frames 120×160), which is widely employed in different tasks like tracking and background extraction. UCSD (with frames 152×242) includes 18 video sequences with complex stations in real-word, some scenes have various moving objects like crowds, ranging from sparse to very crowded even in a series of the frame. CDnet (with frames 240×320) is another video dataset utilized for evaluating change and motion detection methods, which include some given dynamic background like water waves and tremble leaves. LASIESTA (with frames 288×352) is the latest dataset for background removal, which is composed of various real-world indoor and outdoor frame sequence with some challenging situation, such as the prospect of staying immobile for some time.

To quantitatively evaluate the superiority and inferiority of these methods, we introduce the concept of precision, recall, and F-score, which are defined as

$$R = \frac{TP}{TP + FN}, P = \frac{TP}{TP + FP}, F = 2 \frac{R \cdot P}{R + P}.$$

Here, TP represents the percent of true foreground pixels that are recovered, FP represents the percent of true background pixels that are wrongly detected, FN represents the percent of true foreground pixels that are missed. Thus, the evaluation index recall and precision are denoted as R and P, respectively. Finally, F-score is defined to balance R and P. Obviously, a higher F-score implies better background subtraction.

The quantitative results of these compared methods are provided in Table 6, where the highest F-score values are labeled in bold. Compared with other methods, the proposed MCJSL obtains the highest F-score in all cases. For further discussion, Fig. 8 and Fig. 9 show the extracting foreground, where red regions are drawn for missing pixels and blue regions are drawn for false detection. It can be observed that, in Fig. 8, ManiDec and our proposed method work efficiently when facing with these noise background like waves and disturbances. However, ManiDec may have some holes shown as red regions like Fountain and Chopper. Fig. 9 visualizes the results on the LASIESTA dataset, which is more challenging due to decentralized multiple dynamic objectives and cluttered

Table 6
Results of R, P and F-score belong to various methods.

Samples	Boats			Overpass			Fountain			Chopper			Average		
	P	R	F	P	R	F	P	R	F	P	R	F	P	R	F
MOG	0.27	0.83	0.40	0.23	0.82	0.36	0.29	0.92	0.44	0.48	0.87	0.62	0.32	0.86	0.46
FPCP	0.68	0.57	0.62	0.81	0.60	0.69	0.85	0.72	0.78	0.68	0.69	0.68	0.76	0.65	0.69
VB	0.29	0.83	0.42	0.25	0.83	0.38	0.32	0.92	0.47	0.49	0.81	0.61	0.34	0.85	0.47
DECOLOR	0.27	0.84	0.41	0.27	0.80	0.40	0.35	0.93	0.51	0.59	0.88	0.71	0.37	0.86	0.51
BRMF	0.27	0.83	0.40	0.22	0.86	0.35	0.32	0.93	0.47	0.57	0.89	0.69	0.35	0.88	0.48
GoDec	0.25	0.84	0.39	0.68	0.54	0.60	0.28	0.92	0.42	0.41	0.93	0.57	0.41	0.81	0.50
FW-T	0.37	0.77	0.50	0.47	0.75	0.58	0.67	0.82	0.74	0.57	0.76	0.65	0.52	0.78	0.62
WNNM	0.84	0.83	0.82	0.62	0.74	0.67	0.85	0.95	0.90	0.67	0.70	0.69	0.75	0.81	0.77
ManiDec	0.87	0.86	0.83	0.82	0.74	0.75	0.88	0.93	0.91	0.75	0.75	0.74	0.83	0.82	0.81
MCJSL	0.99	0.75	0.85	0.97	0.74	0.84	0.94	0.92	0.93	0.80	0.80	0.93	0.80	0.80	0.86
Samples	Shadow			Cars			Pedestrian			Snow			Average		
	P	R	F	P	R	F	P	R	F	P	R	F	P	R	F
MOG	0.22	1.00	0.36	1.00	0.80	0.89	0.91	0.77	0.83	0.51	0.71	0.59	0.66	0.82	0.67
FPCP	0.22	1.00	0.36	0.99	0.57	0.72	0.94	0.50	0.66	0.94	0.39	0.56	0.77	0.62	0.58
VB	0.20	1.00	0.33	0.98	0.90	0.94	0.80	0.84	0.82	0.67	0.79	0.72	0.66	0.88	0.70
DECOLOR	0.23	1.00	0.37	0.99	0.90	0.94	0.79	0.85	0.82	0.66	0.49	0.57	0.67	0.81	0.68
PRMF	0.23	1.00	0.38	0.97	0.91	0.94	0.65	0.83	0.73	0.45	0.86	0.59	0.58	0.90	0.66
GoDec	0.14	1.00	0.25	0.89	0.66	0.75	0.34	0.84	0.48	0.55	0.82	0.66	0.48	0.83	0.54
FW-T	0.45	1.00	0.62	1.00	0.80	0.89	0.91	0.77	0.83	0.83	0.70	0.76	0.80	0.82	0.78
WNNM	0.73	0.99	0.84	0.98	0.89	0.93	0.92	0.82	0.87	0.69	0.93	0.79	0.83	0.91	0.86
ManiDec	0.76	0.97	0.86	0.98	0.90	0.94	0.94	0.86	0.89	0.71	0.92	0.82	0.85	0.91	0.88
MCJSL	0.85	0.95	0.90	0.98	0.93	0.96	0.87	0.98	0.92	0.84	0.89	0.87	0.89	0.94	0.91

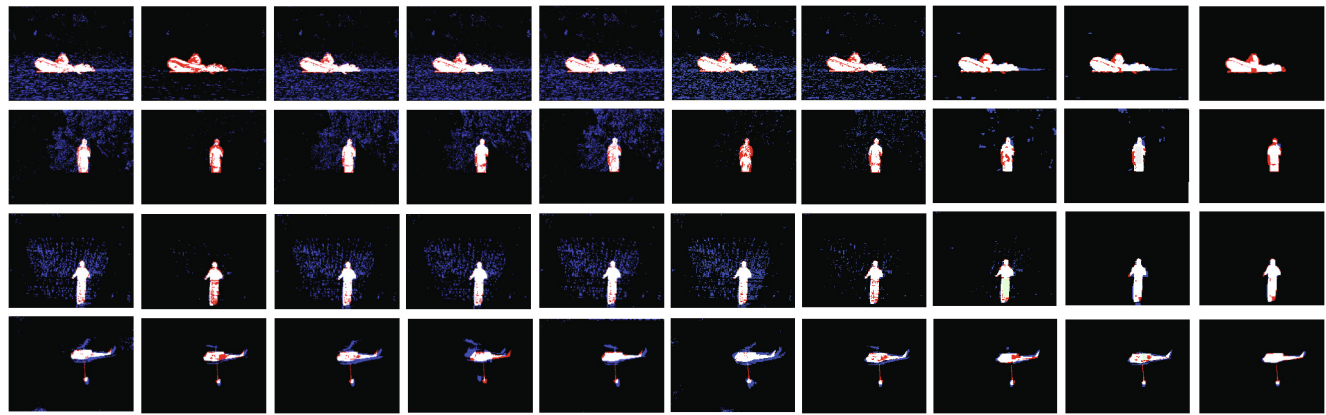


Fig. 8. Background subtraction results on CDnet, I2R, UCSD datasets. From left to right: Ground truth, MOG, FPCP, VBRPCA, DECOLOR, PRMF, GoDec, FW-T, WNNM, ManiDec and MCJSL.

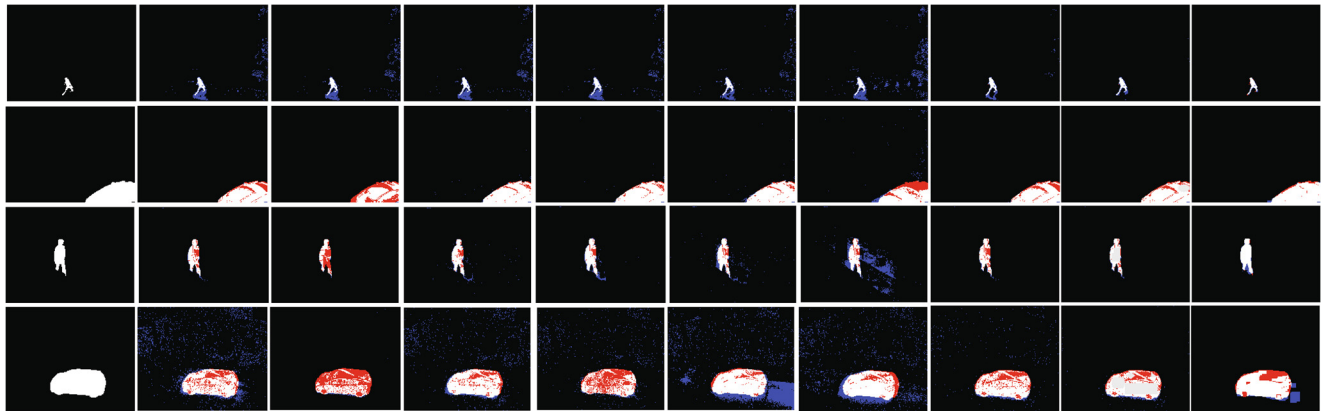


Fig. 9. Background subtraction results on LASIESTA dataset. From left to right: Ground truth, MOG, FPCP, VBRPCA, DECOLOR, PRMF, GoDec, FW-T, WNNM, ManiDec and MCJSL.

backgrounds. All the above methods can extract dynamic foreground from video sequences with differences in visualization, especially the elimination of noise, dynamic background. It can be obviously discovered that the proposed MCJSL performs better on the integrity of foreground extraction. These results prove the robustness of our algorithm in various complex scenes. However, for high-resolution video frames (with frames 1280×720 or above), or for multiple moving objects appearing simultaneously,

our technique can not be utilized for real-time processing, which should be considered in the future.

5.3. Convergence analysis

In Fig. 10, the relative errors of low-rank matrix \mathbf{L} and sparse matrix \mathbf{S} are plotted. When the number of iterations increases, both of the relative differences decrease rapidly, which signifies that the proposed algorithm converges after finite number of iterations. It validates that MCJSL is efficient and convergent.

6. Conclusions

In this paper, a manifold constrained joint sparse learning (MCJSL) approach is proposed, in which the manifold learning and non-convex regularization are explicitly introduced to constrain continuous spatiotemporal sequences. Technically, the manifold constraints are embedded in the process of low-rank and sparse learning. An effective algorithm for solving the MCJSL is constructed with convergence analysis. The extensive experimental results on image denoising and background subtraction show the efficacy of our method. In particular, the denoising performance is increased by 0.03 dB–0.17 dB on average.

Although the proposed MCJSL achieves satisfactory performance for image denoising and background subtraction, several interesting and important questions remain open. On one hand, the present method is only developed intuitively based on real-world application, how to accelerate the algorithm should be further considered theoretically and numerically. On the other hand, for some extreme cases, this method does not perform well, hence extending the model with deep neural networks or transfer learning is necessary and promising.

CRediT authorship contribution statement

Jingjing Liu: Conceptualization, Methodology, Writing – original draft, Writing – review & editing. **Xianchao Xiu:** Supervision, Writing – review & editing. **Xin Jiang:** Writing – original draft. **Wanquan Liu:** Validation, Writing – review & editing. **Xiaoyang Zeng:** Supervision, Writing – review & editing. **Mingyu Wang:** Investigation. **Hui Chen:** Data curation, Validation.

Declaration of competing interest

The authors declare that they have no known competing financial interests or personal relationships that could have appeared to influence the work reported in this paper.

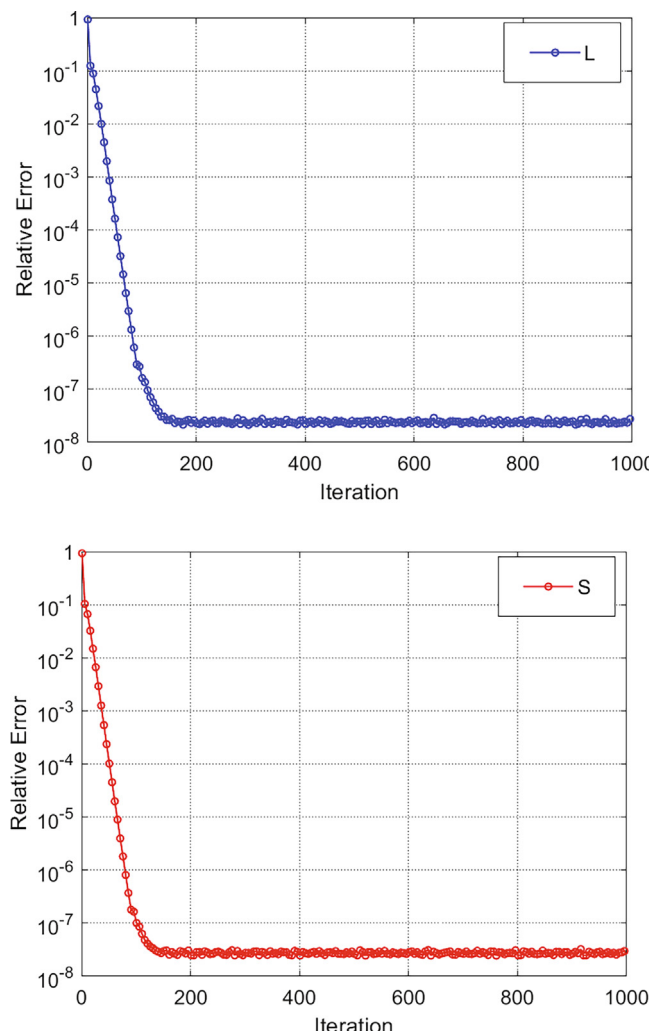


Fig. 10. The relative error of \mathbf{L} and \mathbf{S} .

Acknowledgments

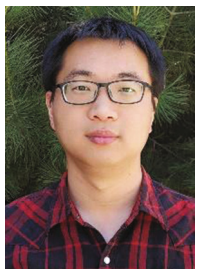
This work was partially supported by the National Natural Science Foundation of China under Grant Nos. (12001019, 62074041), and the Natural Science Foundation of Shanghai under Grant Nos. (19ZR1420800, 20ZR1421300). The authors would like to thank the associate editor and three anonymous reviewers for their numerous insightful comments, which have greatly improved the article.

References

- [1] B. Hong, L. Wei, Y. Hu, D. Cai, X. He, Online robust principal component analysis via truncated nuclear norm regularization, *Neurocomputing* 175 (2016) 216–222.
- [2] X. Shi, F. Nie, Z. Lai, Z. Guo, Robust principal component analysis via optimal mean by joint $L_{2,1}$ and Schatten p-norms minimization, *Neurocomputing* 283 (2018) 205–213.
- [3] X. Xie, J. Wu, G. Liu, J. Wang, Matrix recovery with implicitly low-rank data, *Neurocomputing* 334 (2019) 219–226.
- [4] C. Jiang, F. Zhang, J. Wang, C.-Y. Yang, W. Wang, Robust principal component analysis with intra-block correlation, *Neurocomputing* 386 (2020) 165–178.
- [5] Q. Wang, Q. Gao, G. Sun, C. Ding, Double robust principal component analysis, *Neurocomputing* 391 (2020) 119–128.
- [6] B. Garcia-Garcia, T. Bouwmans, A.J.R. Silva, Background subtraction in real applications: Challenges, current models and future directions, *Comput. Sci. Rev.* 35 (2020) 100204.
- [7] G. Liu, Z. Lin, S. Yan, J. Sun, Y. Yu, Y. Ma, Robust recovery of subspace structures by low-rank representation, *IEEE Trans. Pattern Anal. Mach. Intell.* 35 (1) (2012) 171–184.
- [8] D. Gross, Recovering low-rank matrices from few coefficients in any basis, *IEEE Trans. Inf. Theory* 57 (3) (2011) 1548–1566.
- [9] E.J. Candès, X. Li, Y. Ma, J. Wright, Robust principal component analysis?, *J. ACM (JACM)* 58 (3) (2011) 1–37.
- [10] T. Bouwmans, E.H. Zahzah, Robust PCA via principal component pursuit: A review for a comparative evaluation in video surveillance, *Comput. Vis. Image Underst.* 122 (2014) 22–34.
- [11] X. Xiu, Y. Yang, L. Kong, W. Liu, Laplacian regularized robust principal component analysis for process monitoring, *J. Process Control* 92 (2020) 212–219.
- [12] J. Liu, R. Ma, X. Zeng, W. Liu, M. Wang, H. Chen, An efficient non-convex total variation approach for image deblurring and denoising, *Appl. Math. Comput.* 397 (2021) 125977.
- [13] J.-F. Cai, E.J. Candès, Z. Shen, A singular value thresholding algorithm for matrix completion, *SIAM J. Optim.* 20 (4) (2010) 1956–1982.
- [14] S. Gu, Q. Xie, D. Meng, W. Zuo, X. Feng, L. Zhang, Weighted nuclear norm minimization and its applications to low level vision, *Int. J. Comput. Vision* 121 (2) (2017) 183–208.
- [15] Y. Hu, D. Zhang, J. Ye, X. Li, X. He, Fast and accurate matrix completion via truncated nuclear norm regularization, *IEEE Trans. Pattern Anal. Mach. Intell.* 35 (9) (2012) 2117–2130.
- [16] K.G. Quach, C.N. Duong, K. Luu, T.D. Bui, Non-convex online robust PCA: Enhance sparsity via L_p -norm minimization, *Comput. Vis. Image Underst.* 158 (2017) 126–140.
- [17] A. Parekh, I.W. Selesnick, Improved sparse low-rank matrix estimation, *Signal Processing* 139 (2017) 62–69.
- [18] W. Chen, Simultaneously sparse and low-rank matrix reconstruction via nonconvex and nonseparable regularization, *IEEE Trans. Signal Process.* 66 (20) (2018) 5313–5323.
- [19] F. Wen, R. Ying, P. Liu, R.C. Qiu, Robust PCA using generalized nonconvex regularization, *IEEE Trans. Circuits Syst. Video Technol.* 30 (6) (2019) 1497–1510.
- [20] S. Wang, K. Xia, L. Wang, J. Zhang, H. Yang, Improved RPCA method via non-convex regularisation for image denoising, *IET Signal Proc.* 14 (5) (2020) 269–277.
- [21] J. Liu, S. Ji, J. Ye, Multi-task feature learning via efficient $L_{2,1}$ -norm minimization, *arXiv:1205.2631*.
- [22] X. Xiu, Y. Yang, L. Kong, W. Liu, Data-driven process monitoring using structured joint sparse canonical correlation analysis, *IEEE Trans. Circuits Syst. II Express Briefs* 68 (1) (2020) 361–365.
- [23] S.T. Roweis, L.K. Saul, Nonlinear dimensionality reduction by locally linear embedding, *Science* 290 (5500) (2000) 2323–2326.
- [24] Y. Liu, J. Zeng, L. Xie, S. Luo, H. Su, Structured joint sparse principal component analysis for fault detection and isolation, *IEEE Trans. Industr. Inf.* 15 (5) (2018) 2721–2731.
- [25] J. Liu, D. He, X. Zeng, M. Wang, X. Xiu, W. Liu, W. Li, ManiDec: Manifold Constrained Low-Rank and Sparse Decomposition, *IEEE Access* 7 (2019) 112939–112952.
- [26] Z. Xu, X. Chang, F. Xu, H. Zhang, $L_{1/2}$ regularization: A thresholding representation theory and a fast solver, *IEEE Trans. Neural Networks and Learn. Syst.* 23 (7) (2012) 1013–1027.
- [27] J.B. Tenenbaum, D. Silva, V.J.C. Langford, A global geometric framework for nonlinear dimensionality reduction, *Science* 290 (5500) (2000) 2319–2323.
- [28] J. Chen, R. Wang, S. Yan, S. Shan, X. Chen, W. Gao, Enhancing human face detection by resampling examples through manifolds, *IEEE Trans. Syst. Man Cybern. Part A: Syst. Hum.* 37 (6) (2007) 1017–1028.
- [29] J. Fan, R. Li, Variable selection via nonconcave penalized likelihood and its oracle properties, *J. Am. Stat. Assoc.* 96 (456) (2001) 1348–1360.
- [30] Y. Chen, N. Xiu, D. Peng, Global solutions of non-Lipschitz $S_2 - S_p$ minimization over the positive semidefinite cone, *Optim. Lett.* 8 (7) (2014) 2053–2064.
- [31] M. Yuan, Y. Lin, Model selection and estimation in regression with grouped variables, *J. R. Stat. Soc.: Ser. B (Statist. Methodol.)* 68 (1) (2006) 49–67.
- [32] L. Yang, T.K. Pong, X. Chen, Alternating direction method of multipliers for a class of nonconvex and nonsmooth problems with applications to background/foreground extraction, *SIAM J. Imaging Sci.* 10 (1) (2017) 74–110.
- [33] K. Dabov, A. Foi, V. Katkovnik, K. Egiazarian, Image denoising by sparse 3-D transform-domain collaborative filtering, *IEEE Trans. Image Process.* 16 (8) (2007) 2080–2095.
- [34] J. Mairal, F. Bach, J. Ponce, G. Sapiro, A. Zisserman, Non-local sparse models for image restoration, in: *IEEE 12th International Conference on Computer Vision* (2009) 2272–2279.
- [35] W. Dong, L. Zhang, G. Shi, Centralized sparse representation for image restoration, *Int. Conf. Computer Vis.* (2011) 1259–1266.
- [36] W. Dong, G. Shi, X. Li, Nonlocal image restoration with bilateral variance estimation: a low-rank approach, *IEEE Trans. Image Process.* 22 (2) (2012) 700–711.
- [37] A. Levin, B. Nadler, Natural image denoising: Optimality and inherent bounds, *Int. Conf. Comput. Vis.* (2011) 2833–2840.
- [38] D.L. Donoho, De-noising by soft-thresholding, *IEEE Trans. Inf. Theory* 41 (3) (1995) 613–627.
- [39] Q. Zhao, D. Meng, Z. Xu, W. Zuo, L. Zhang, Robust principal component analysis with complex noise, *Int. Conf. Mach. Learn.* (2014) 55–63.
- [40] P. Rodriguez, B. Wohlberg, Fast principal component pursuit via alternating minimization, *IEEE Int. Conf. Image Process.* (2013) 69–73.
- [41] S.D. Babacan, M. Luessi, R. Molina, A.K. Katsaggelos, Sparse Bayesian Methods for Low-Rank Matrix Estimation, *IEEE Trans. Signal Process.* 60 (8) (2012) 3964–3977.
- [42] Z. Xiaowei, Y. Can, Y. Weichuan, Moving Object Detection by Detecting Contiguous Outliers in the Low-Rank Representation, *IEEE Trans. Pattern Anal. Mach. Intell.* 35 (3) (2013) 597–610.
- [43] X. Zhou, C. Yang, W. Yu, Automatic mitral leaflet tracking in echocardiography by outlier detection in the low-rank representation, *IEEE Conf. Comput. Vis. Pattern Recognit.* (2012) 972–979.
- [44] N. Wang, T. Yao, J. Wang, D.-Y. Yeung, A probabilistic approach to robust matrix factorization (2012) 126–139.
- [45] A. Sobral, T. Bouwmans, E.-H. Zahzah, Lrslibrary: Low-rank and sparse tools for background modeling and subtraction in videos, *Robust Low-Rank and Sparse Matrix Decomposition: Applications in Image and Video Processing*, .
- [46] C. Mu, Y. Zhang, J. Wright, D. Goldfarb, Scalable robust matrix recovery: Frank-Wolfe meets proximal methods, *SIAM J. Sci. Comput.* 38 (5) (2016) A3291–A3317.
- [47] L. Li, W. Huang, I.Y.-H. Gu, Q. Tian, Statistical modeling of complex backgrounds for foreground object detection, *IEEE Trans. Image Process.* 13 (11) (2004) 1459–1472.
- [48] N. Goyette, P.-M. Jodoin, F. Porikli, J. Konrad, P. Ishwar, Chagedetection.net: A new change detection benchmark dataset, in: *IEEE computer society conference on computer vision and pattern recognition workshops* (2012) 1–8..
- [49] C. Guo, Q. Ma, L. Zhang, Spatio-temporal saliency detection using phase spectrum of quaternion fourier transform, in: *IEEE Conference on Computer Vision and Pattern Recognition*, 2008, pp. 1–8.
- [50] C. Cuevas, E.M. Yáñez, N. García, Tool for semiautomatic labeling of moving objects in video sequences: TSLAB, *Sensors* 15 (7) (2015) 15159–15178.



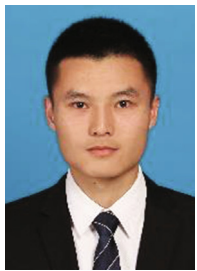
Dr. Jingjing Liu received her Bachelor degree in Electrical Engineering from Zhengzhou University, P.R. China, in 2002, the MSc and PhD degree in Control Science and Engineering at Shanghai University in 2010. She was a joint PhD in Computation department of Curtin University in Australia from December 2015 to December 2016. Currently, she is a candidate of Postdoctoral at the State Key Laboratory of ASIC and System, Fudan University with interests in pattern recognition, computer vision, machine learning and control systems.



Dr. Xianchao Xiu received his Bachelor degree in Applied Mathematics from Hebei North University, P.R. China, in 2011, the MSc and PhD degree in Control Theory and Operation Research from Beijing Jiaotong University in 2014 and 2019 respectively. He is currently a post Doctor in State Key Lab for Turbulence and Complex Systems at Peking University. His current research interests include large-scale sparse optimization, signal processing, machine learning, and fault detection.



Prof. Xiaoyang Zeng received his PhD degree from Chinese Academy of Sciences in 2001. He is currently the executive director of the State Key Laboratory of ASIC and System, the vice dean of the School of Microelectronics of Fudan University. He also serves as the co-chair of the Circuit & System Division of Chinese Institute of Electronics, the steering committee member of ASP-DAC, the TPC Member of A-SSCC, also the TPC Chair of ASICON 2009/2013. His research fields include high-performance and low-power VLSI architecture design for information security algorithms, digital signal processing algorithms, wireless communication base-band processing, and the mixed-signal circuits design technology.



Mr. Xin Jiang obtained his Bachelor degree in Micro-electronic from Harbin Institute of Technology, P.R. China, in 2019. He is a candidate of Master at the State Key Laboratory of ASIC and System, Fudan University, Shanghai, China with the interests in machine learning algorithm. His current research direction also includes the design of digital integrated circuits based on intelligent algorithms.



Prof. Mingyu Wang received the B.S. degree from the Huazhong University of Science and Technology, Wuhan, China, in 1999, the M.S. degree in electronic engineering from Shanghai Jiaotong University, China, in 2001, and the PhD. degree from the School of Microelectronics, Fudan University, Shanghai, China, in 2011. He currently serves as an associate Professor with the State Key Laboratory of ASIC and System, Fudan University. His research interests include artificial intelligence chip design, mixed signal circuit design, and low power SOC design.



Prof. Wanquan Liu received the BSc degree in Applied Mathematics from Qufu Normal University, P.R. China, in 1985, the MSc degree in Control Theory and Operation Research from Chinese Academy of Science in 1988, and the PhD degree in Electrical Engineering from Shanghai Jiaotong University, in 1993. He once held the ARC Fellowship, U2000 Fellowship and JSPS Fellowship and attracted research funds from different resources over 2.4 million dollars. He is currently an Associate Professor in the Department of Computing at Curtin University and is in editorial board for nine international journals. His current research interests include large-scale pattern recognition, signal processing, machine learning, and control systems.



Dr. Hui Chen received the B.S. degree in measurement and control technology and instrument from Jiangsu University in 2006. She received her M.S.degree in measurement and control technology and instrument from Shanghai University in 2009 and her doctor degree in control theory and control engineering from Shanghai University in 2014. She was a visiting Ph.D. Student in the field of robotic in Irseem ESIGELEC, France and Jacobs University Bremen, Germany from 2010 to 2012. She is currently an associate professor in Shanghai University Electric Power. Her research interests include control engineering, computer vision, image processing, and robot navigation.